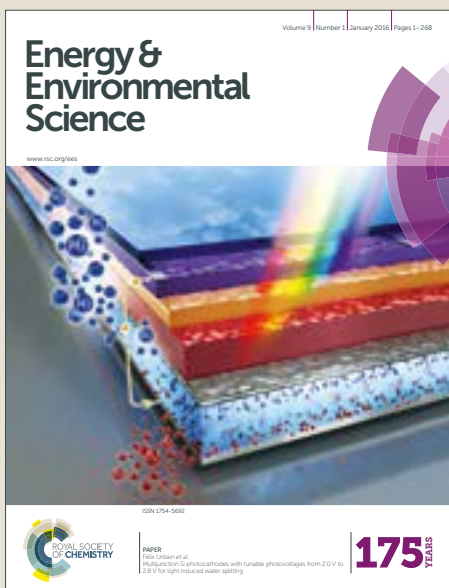


Energy & Environmental Science

Accepted Manuscript



This article can be cited before page numbers have been issued, to do this please use: J. Mao, J. Icozzia, J. Huang, K. Meng, Y. Lai and Z. Lin, *Energy Environ. Sci.*, 2018, DOI: 10.1039/C7EE03031B.



This is an Accepted Manuscript, which has been through the Royal Society of Chemistry peer review process and has been accepted for publication.

Accepted Manuscripts are published online shortly after acceptance, before technical editing, formatting and proof reading. Using this free service, authors can make their results available to the community, in citable form, before we publish the edited article. We will replace this Accepted Manuscript with the edited and formatted Advance Article as soon as it is available.

You can find more information about Accepted Manuscripts in the [author guidelines](#).

Please note that technical editing may introduce minor changes to the text and/or graphics, which may alter content. The journal's standard [Terms & Conditions](#) and the ethical guidelines, outlined in our [author and reviewer resource centre](#), still apply. In no event shall the Royal Society of Chemistry be held responsible for any errors or omissions in this Accepted Manuscript or any consequences arising from the use of any information it contains.

Journal Name**ARTICLE****Graphene Aerogels for Efficient Energy Storage and Conversion**Jiajun Mao^{a†}, James Icozzia^{b†}, Jianying Huang^{a‡}, Kai Meng^a, Yuekun Lai^{a,*} and Zhiqun Lin^{b,*}Received 00th January 20xx,
Accepted 00th January 20xx

DOI: 10.1039/x0xx00000x

www.rsc.org/

Concerns over air quality reduction resulting from burning fossil fuels have driven the development of clean and renewable energy sources. Supercapacitors, batteries and solar cells serve as eco-friendly energy storage and conversion systems vitally important for the sustainable development of human society. However, many diverse elements influence the performance of energy storage and conversion systems. The overall efficiency of systems depends on the specific structure and properties of incorporated functional materials. Carbon materials, such as graphene, are especially promising for materials development in the energy storage and conversion fields. Graphene, a two-dimensional (2D) carbon material only a single atomic thick, has massless Dirac fermions (electron transport is governed by Dirac's equation), displays outstanding electrical conductivity, superior thermal conductivity and excellent mechanical properties. 2D free-standing graphene films and powders have paved the way for promising energy applications. Recently, much effort has been spent trying to improve the number of active sites in electrode materials within 3D network/aerogel structures derived from graphene. This is because graphene aerogels are promising materials for energy systems due to their porous hierarchical structure which affords rapid electron/ion transport, superior chemical and physical stability, and good cycle performance. This review aims to summarize the synthetic methods, mechanistic aspects, and energy storage and conversion applications of novel 3D network graphene, graphene derivatives and graphene-based materials. Areas of application include supercapacitors, Li-batteries, H₂ and thermal energy storage, fuel cells and solar cells.

Introduction

The Environmental pollution caused by the rapid consumption of fossil fuels in many developing countries has prompted necessary investigation into alternative sources of energy. The rapid consumption of fossil fuels produces large amounts of toxic SO_x, NO_x, and other volatile organic compounds resulting in dangerous levels of fine particulate matter (PM_{2.5}) as well as large amounts of greenhouse gases such as CO₂, CH₄, and chlorofluorocarbons.¹⁻³ In conjunction with their non-renewable nature and increasingly limited easy availability, several estimates have concluded that our reserves may be depleted in as few as 100 years based on current consumption trends. Therefore the development of clear, low-cost, and sustainable energy sources cannot be more urgent.⁴⁻⁹ Supercapacitors, Li-batteries, fuel cells and solar cells are several green and renewable energy systems which have received various degrees of industrial success while also

satisfying the energy requirements of modern life.¹⁰⁻¹⁴ However, there are many factors that influence the efficiency of these energy systems (i.e. the amount of electricity generated for a given amount of incident energy input). Maximizing the efficiency is one of the most important challenges dictating the success of any renewable energy technology and it is largely dependent on the structure and properties of candidate materials.

Nanotechnology takes advantage of the significant relationship between properties and structure size that occurs on the nanoscale in materials from 0D to 3D complexity. In addition the properties of nanostructured materials are often vastly different from familiar bulk counterparts. Possessing a single atomic carbon thickness and massless Dirac fermions, sheet-like (2D) graphene derivatives have attracted great interest for energy applications due to their outstanding photoelectrochemical performance. With these in mind, the rational assembly of nano-sheets into macroscopic structures which afford large internal reactive area and direct molecular transport are vital factors to realize the rapid development of energy storage and conversion. 3D network aerogel morphologies are a framework containing interconnected micro-/nanosheets while also possessing hierarchical pores on micro, meso, and macro scales in contrast to 2D films. The micro and mesopores structures contribute to the high special surface area and the macropores provide accessibility to the active surfaces. At the same time, the ultralow density and flexibility

^a National Engineering Laboratory for Modern Silk, College of Textile and Clothing Engineering, Soochow University, Suzhou 215123, P. R. China. E-mail: yklai@suda.edu.cn

^b School of Materials Science and Engineering, Georgia Institute of Technology, Atlanta, Georgia 30332, USA. E-mail: zhiqun.lin@mse.gatech.edu

† Footnotes relating to the title and/or authors should appear here.

Electronic Supplementary Information (ESI) available: [details of any supplementary information available should be included here]. See DOI: 10.1039/x0xx00000x

ARTICLE

Journal Name

of 3D aerogels are beneficial for portable electronics affording excellent mechanical stability and high flexural strength. In addition to structure and morphology, the electronic and chemical properties are important in all applications. For example, graphene has a high specific surface area ($\sim 2800 \text{ m}^2 \text{ g}^{-1}$), superior electrical conductivity ($\sim 10^6 \text{ S cm}^{-1}$), excellent thermal conductivity ($\sim 6000 \text{ W m}^{-1} \text{ K}^{-1}$), and ultra-low optical absorption (2.3%). When combined with other nano and micron materials, the resulting composites can combine desirable bulk properties and processability with the unique nanoscale properties described above.

Owing to their numerous conductive interconnections between 2D sheets, graphene aerogels and their composites are promising for various energy systems. Among energy storage devices, supercapacitors typically have high power densities and low energy densities (i.e. a small water jug with a large spout). In contrast, batteries typically have high energy densities but low power densities (i.e. a large water jug with a small spout). Ideal storage devices should possess high power and energy densities as well as quick charging/recharging, and long cycle life. Superior conductivity and specific graphene aerogel morphologies contribute to a qualitative leap in performance and applicability because the hierarchical porosity and high contact area satisfy the requirement for a large number of stored charges as well as the rapid transport of ions/electrons during the reversible charge/discharge processes. The robust graphene aerogel 3D network provides physical and chemical stability during repeated ion intercalation and deintercalation enabling long cycle lifetimes for graphene aerogel-based devices. For fuel cells or metal-air batteries, water splitting, oxygen reduction reaction (ORR), oxygen evolution reaction (OER) and hydrogen evolution reaction (HER) are crucial half-electrochemical processes that occur. Noble metals (Pd, Au, and Pt) and transition-metal oxides (TiO_2 , and RuO_2) are the most wildly used catalysts. However they are not ideal due to high costs as well as toxicity both of which greatly hinder their development. Owing to the large number of active sites, high conductivity and metal-free composition (i.e. low cost), graphene aerogel-based materials are attractive for electro-catalytic applications. In dye-sensitized solar cells (DSSCs), graphene aerogels can serve as a counter electrode, a modifier for TiO_2 inverse opal electrodes, and a solid state electrolyte possessing improved power conversion efficiencies due to its quick charge transfer capabilities.

This review will provide an in-depth understanding of graphene aerogel-based materials as they apply to energy systems (supercapacitors, Li-batteries, fuel cells, metal-air batteries, and solar cells). This work will briefly outline and compare various fabrication methods of graphene aerogels and detail the various advantages of graphene aerogels as they apply to each specific device area. In addition, we will look into some critical engineering strategies that give rise to the excellent properties of 3D graphene aerogels such as enlarged surface area, tailored porosity and efficient separation of carriers. Graphene aerogels represent a high performance, low-cost material for near future energy technologies.

2. Fabrication of Graphene Aerogels

[View Article Online](#)

DOI: 10.1039/C7EE03031B

The realization of high performance graphene materials immediately necessitates the nanoscale exfoliation of neighboring sheets into individual layers prior to incorporation into any macrostructure. This section details significant reports dealing with the improvement in the quantity and quality of graphene layers. Many techniques including mechanical stripping,¹⁵ oxidation-reduction method,¹⁶ and chemical vapor deposition (CVD),¹⁷ have been proposed to construct carbon-based nanomaterials. The latter two are the most widely used techniques. The oxidation-reduction method first converts graphite into graphite/graphene oxide through the well-known Hummers' method. After intermediate exfoliation or ultrasonication to produce graphene oxide (GO), it is then reduced by hydrazine hydrate, Vitamin C, isocyanic acid or thermally to yield graphene. CVD harnesses a different carbon source to grow graphene on a variety of substrates such as metallic (Cu, Ni, Co, Fe) or planar nonmetallic surfaces (SiO_2 , Si_3N_4 , SrTiO_3 , NaCl). During a typical CVD treatment, hydrocarbon precursors are pyrolyzed to carbon radicals when they pass through the hot zone and then deposited on the surface where self-limited growth occurs to form a single-layer or few-layer graphene on substrates. Compared to the oxidation-reduction technique, CVD growth has several including an ordered structure, and excellent electronic properties of the resulting graphene nanostructures. However, it requires an extra transfer process to put the graphene layer onto other desired substrates, often accompanied with lower yields and reduced quality.

2D materials manufactured using freestanding graphene nanosheets and modified graphene can be used in sensors, electro chemistry, photocatalysis and filtration. These materials have attracted great interest in recent years.¹⁸⁻²¹ However, there are few reviews related to graphene aerogels which have stable 3D networks and high pore volumes in contrast to conventional graphene films. Monte and coworkers summarized the synthesis and application of carbon nanotubes and graphene aerogels.²² Chen and coworkers investigated the synthesis, properties and application of 3D graphene networks.²³ Building on this previous work, we summarize multiple fabrication techniques for the rational construction of 3D graphene aerogels. Self-assembly strategies are a common "bottom-up" approach. Graphene nanosheets serve as the building blocks for self-assembly to obtain 3D porous networks. Shi et al. successfully fabricated mechanically strong, electrically conductive and thermally stable graphene aerogels by a hydrothermal process (Figure 1a). This is a convenient one-step method.²⁴ However, hydrothermal processes typically occur in a Teflon-lined autoclave requiring high pressures. This hinders large scale synthesis as it is a batch rather than continuous process. Yan et al. prepared graphene aerogels by the mild chemical reduction of GO with various reducing agents under atmospheric pressure in an open system. The resulting graphene aerogels showed good mechanical strength, low density and high electrical conductivity facilitating large scale fabrication (Figure 1b).^{25, 26} Self-assembly is possible because of

the abundance of oxygen-containing functional groups on graphene oxide which enable interaction between various sheets. These groups enhance the presence of π - π stacking among the graphene layers and make the graphene nanosheets hydrophobic. Yu et al. reported graphene aerogels induced by Fe(II) ions at different pH values to obtain free-standing graphene/R-FeOOH and magnetic graphene/Fe₃O₄ aerogels with different functionalities for different applications.²⁶

graphene aerogels with embedded nanoparticles (NPs) endow additional functionalities in graphene aerogels.²⁷ Feng et al. hydrothermally assembled GO dispersions and iron acetate to enable the nucleation and growth of Fe₃O₄ nanoparticles on the graphene surface to yield high surface area Fe₃O₄/graphene aerogel composites (Figure 1d).²⁷ Similarly, other materials have been decorated internally and externally onto graphene aerogels such as hierarchical porous MOFs@GA.²⁸

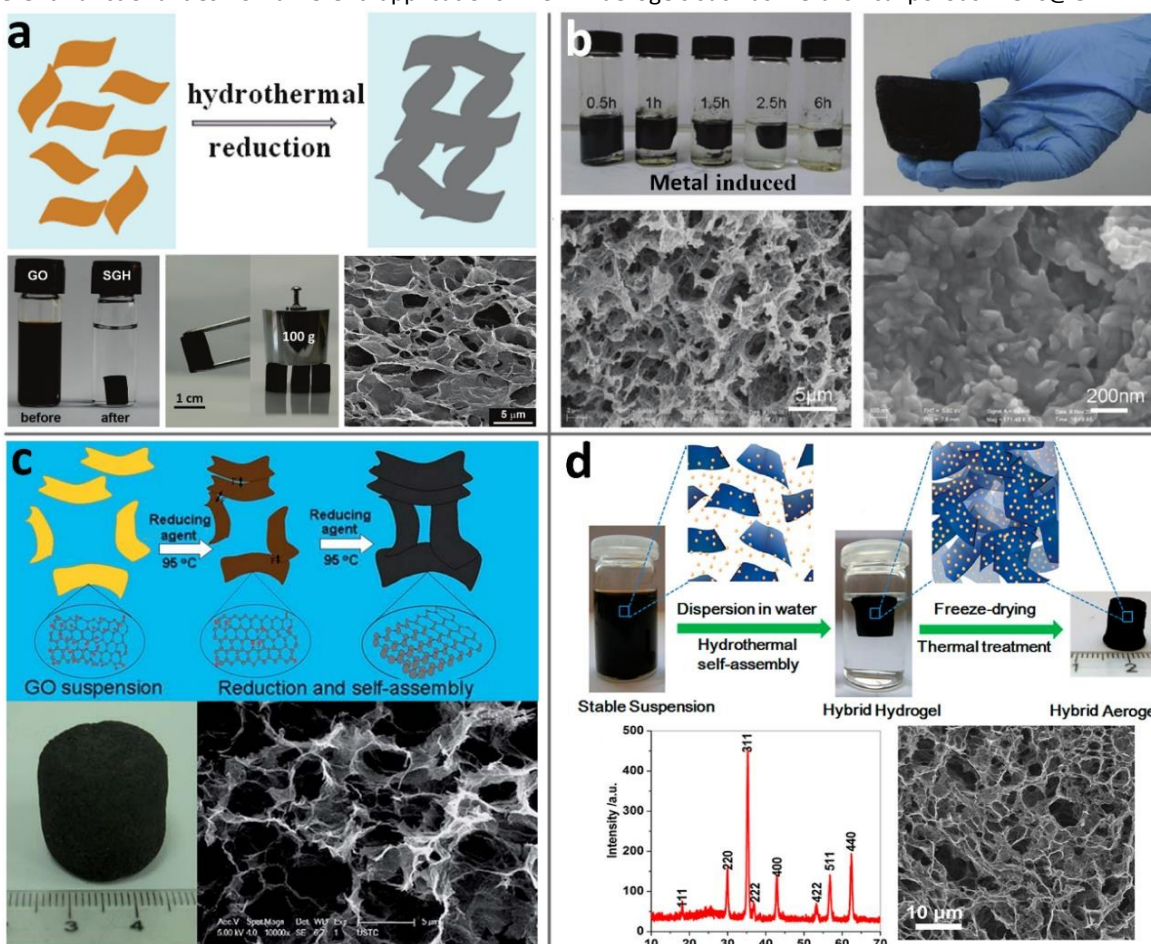


Figure 1. Schematic diagrams of the various techniques employed for the construction of graphene aerogels with corresponding SEM images: (a) hydrothermal reduction self-assembly;²⁴ (b) metal ion-induced self-assembly;²⁶ (c) direct chemical reduction self-assembly;²⁵ (d) hydrothermal self-assembly of Fe₃O₄-containing graphene aerogels.²⁷

Self-assembly strategies offer a convenient and scalable process to manufacture graphene aerogels with good electrical conductivity, and thermal stability. Cross-linkers can also be used to link the graphene layers to form 3D aerogels via electrostatic interaction, hydrogen bonding, and covalent bonding. Cross-linkers provide a more convenient route than direct cryodesiccation from the aqueous state. Gao et al. constructed 3D graphene frameworks with carbon nanotubes (CNTs) using sol cryodesiccation and carbonization. The aerogel had very low density, excellent thermal stability and high absorption (Figure 2a).²⁹ Biopolymers coated with graphene are also beneficial due to their elasticity and fatigue resistance in resulting aerogels. Yu et al. synthesized lamellar chitosan-graphene oxide scaffolds (CS-GO) from a homogeneous mixture via bidirectional freezing and annealing. The resulting

composite showed high compressibility, super-elasticity, and low density (Figure 2b).³⁰ Other cross-linkers, such as sodium dodecyl sulfate,³¹ cellulose,³² and resorcinol-formaldehyde (RF),³³ have also been reported.

Normally, graphene aerogels prepared by self-assembly and cross-linking start with the reduction of graphene oxide. This typically leads to a large number of surface defects and unreduced oxygen-containing groups. CVD-growth is an alternative method that can produce more pristine graphene materials. Zhang et al. obtained high-quality 3D graphene networks using Ni foam templates by the ethanol-CVD method (Figure 2c).³⁴ Templated CVD-growth produces a decent interconnectivity, but the mechanical strength is poor because of the soft pristine graphene framework. Bando et al. developed a template-free strategy for producing 3D graphene aerogel.

ARTICLE

Journal Name

The frameworks are tightly connected and supported by robust graphitic microstructures (Figure 2d).³⁵ In both the templated and template-free strategies, it is possible to ensure that the carbon source converts into 3D graphene aerogel network structures. However, the process is difficult to scale-up. Recently, a 3D printing technique also known as direct ink

writing has been applied in the construction of 3D cellular architectures. Worsley et al. constructed graphene-aerogels³⁶ by a graphene-based direct ink writing process. The as-prepared aerogels were lightweight, highly conductive and highly compressible (Figure 2e).³⁶

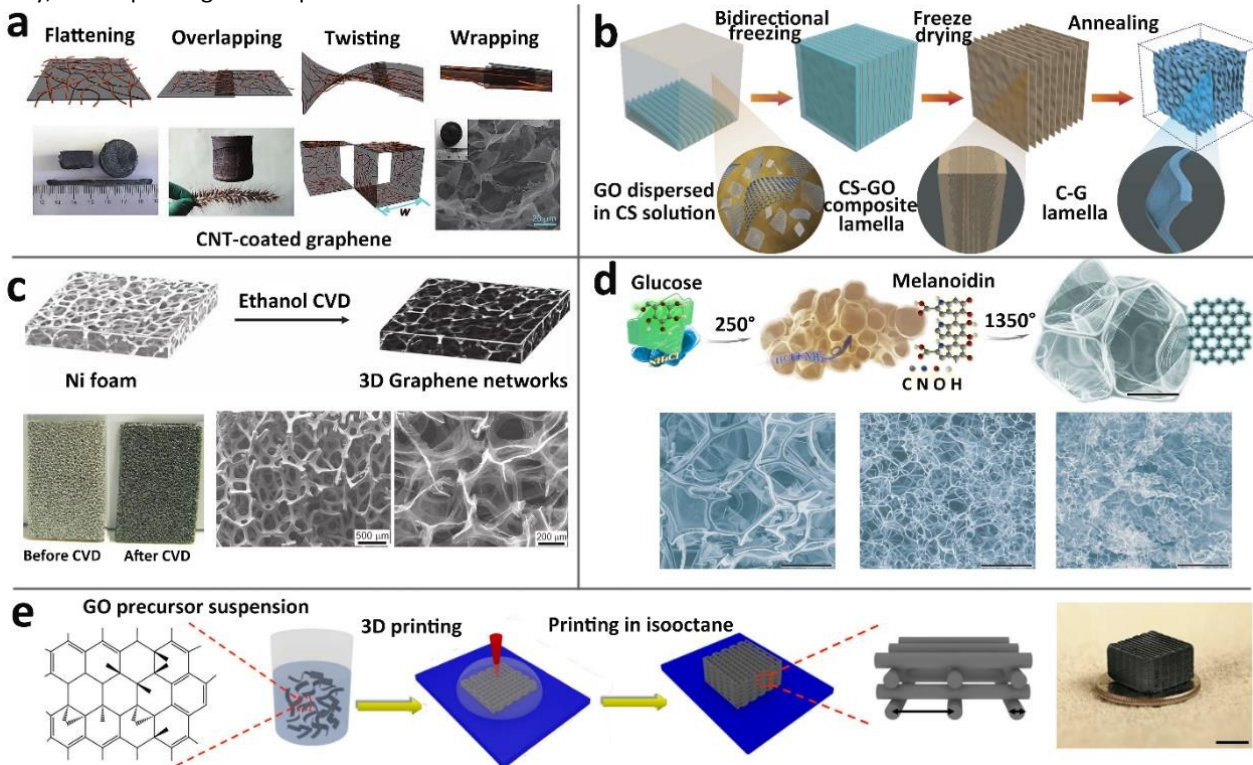


Figure 2. Schematic diagrams of the various fabrication process SEM images of the resulting graphene aerogel morphologies. Synthesis can include (a) carbon nanotube cross-linkers,²⁹ (b) chitosan cross-linkers,³⁰ (c) CVD-growth with Ni foam,³⁴ (d) substrate-free CVD growth,³⁵ and (e) 3D printing.³⁶

3. Mechanisms and Roles of Graphene Aerogels in Energy Storage

Energy storage technology is especially important for mobile applications. For example, cell phones batteries require high energy densities and quick-charging times. Remote controlled drones and electric vehicles also require high gravimetric energy densities and have developed significantly due to their shrinking costs and improved safety. Both supercapacitors and batteries are essential electrochemical energy storage devices that have attracted great attention due to the significant potential improvements that remain. Graphene aerogels and their derivatives functionalized with metal oxides and conductive polymers have been widely used in supercapacitors and batteries.

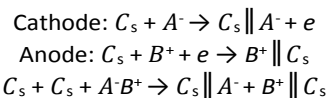
3.1 Supercapacitors

A supercapacitor is one kind of energy storage device filling the gap between batteries and conventional capacitors possessing higher energy densities than conventional capacitors and higher power densities than batteries. Early capacitor designs were composed of a glass insulating medium covered with foil. More recently, mica, ceramic and polystyrene have largely replaced

glass as an insulating medium. Double-layer capacitors appeared in 1957 when General Electric filed the first patent followed by a SOHIO patent about fundamental varieties of supercapacitors at 1962. NEC fabricated market-oriented capacitors in the 1970s and Panasonic manufactured two different supercapacitors including button type and spiral type around the same time. ELIT packaged the first asymmetric capacitors with nickel-metal hydride as the cathode, KOH as the electrolyte, and activated carbon as the anode. Subsequently, multiple supercapacitor types have been optimized for highly specific capacitance and output voltages. Electrochemical adsorption/desorption and redox reactions contribute to the energy storage in supercapacitors. The two storage approaches are highly reversible even high numbers of charge-discharge cycles on the order of hundreds of millions. They have higher power densities on the order of 300-5000 kW kg⁻¹ which are 5-10 times that of Li-ion batteries. Supercapacitors also have superior cycling stability with lifetimes 10-100 times that of batteries. To date, supercapacitors have been widely used in portable electronic devices, electric vehicles, aerospace, and national defense fields for their excellent cycle stability, safety, and rapid charge-discharge performance.

3.1.1 Double-layer Capacitors

Double-layer capacitors (DLCs) are energy storage devices with a double electric layer interface formed between the electrode-active materials and electrolyte for charge storage.^{37, 38} While an external electric field is applied, the positive and negative electrodes, which have stored the corresponding positive and negative charges, gather the opposite ions from the electrolyte to balance the electric field. Potential difference resulting from the migration of ions is mechanism for energy storage. This is a classical physical model of supercapacitors. They are attractive because they possess excellent stability and circulation. The charging process of double-layer capacitors is described by the following equations and Scheme 1b:



Where C_s is the surface of the electrodes, “ \parallel ” is the double-layer cell between the electrodes and electrolyte, and A^- and B^+ represent the anion and cation.

The primary theoretical model was put forward by Helmholtz with the capacitance dictated by the following equation:

$$C = \frac{\epsilon_0 * \epsilon_r}{d} * A$$

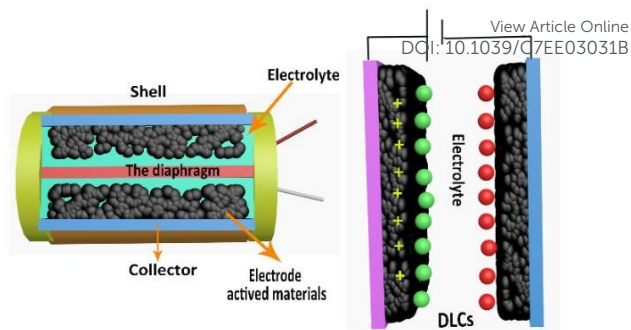
Where ϵ_0 is internal dielectric constant, ϵ_r is the vacuum dielectric constant, A is the surface area of electrode, and d is the effective diameter of cell. This capacitance model was further perfected by dividing the interface of the electrode active materials and electrolyte into a close layer (C_c) which is the layer occurring on polarization at the electrode-electrolyte interface and diffusion layer (C_{diff}) which is the layer forming from the accumulation of ions close to the electrode surface. In this framework, a double-layer capacitor is essentially equal to a series connection of a close layer capacitor and diffusion layer capacitor as follows:

$$\frac{1}{C_{dl}} = \frac{1}{C_c} + \frac{1}{C_{diff}}$$

The cell voltage (V) plays a significant role both in the specific energy and the power of supercapacitors because the stored energy (E) and power (P) are related to the voltage by the following:

$$E = \frac{1}{2} CV^2, P = \frac{V^2}{4R}$$

Despite the fact that aqueous alkaline and acid solutions possess high ionic conductivity and low cost, organic electrolytes are still widely utilized because they can endure higher operation voltages and thus store more energy and have larger power (alkaline or acid electrolytes ~1.23 V, organic electrolytes ~ 2.7 V).



Scheme 1. Schematic diagram of typical double layer capacitors (DLCs).

Electrode interfacial contact, electrode active material type, and their Brunauer-Emmett-Teller specific surface (BET) are key properties in capacitor research.^{39, 40} Graphene is a promising electrode material due to its high BET and conductivity.⁴¹⁻⁴⁴ Ruoff et al. developed symmetrical double-layer capacitors with modified hydrazine hydrate-reduced graphene. The graphene BET reached $705 \text{ m}^2 \text{ g}^{-1}$ with a capacitance 135 F g^{-1} . Such high performance measures are a testament to graphene's applicability in supercapacitors.³⁷

However, graphene powders and films have a tendency to aggregate, often leading to lower BET values. Graphene aerogel, with its high pore volume, enhances the contact area between the network and electrolyte. Shi et al. synthesized graphene hydrogels via a hydrothermal method. Capacitance values reached as high as 160 F/g and were attributed to the macroporous 3D network structure of the graphene.²⁴ Subsequently, the hydrogel was further reduced by hydrazine leading to an increased capacitance of 222 F g^{-1} .⁴⁵ The performance enhancement is attributed to the reduction of oxygen-containing groups which enhance the conductivity from 0.005 S cm^{-1} to 0.032 S cm^{-1} . A higher conductivity represents a higher electronic mobility and higher output power potential. Similarly, Luand et al. developed graphene aerogels with ethylenediamine (EDA) cross-links which when reduced achieved conductivities of 13.51 S cm^{-1} and specific capacitances of 231 F g^{-1} .⁴⁶ In addition, recent work has shown that thermal treatment under inert gasses can yield highly-conductive graphene aerogels analogous to chemical reduction.⁴⁷⁻⁴⁹ Doping graphene with one or several elements such as S, N, B, and P can restructure the graphene crystal lattice and locally manipulate the electronic structures resulting in beneficial chemical and physical changes that can improve the performance of graphene.⁵⁰⁻⁵³ To date, nitrogen is the most popular dopant due to its abundance and ease of incorporation. There are a variety of nitrogen units that can form when graphene is treated with nitrogen plasma including pyridine, pyrrole and nitrogen-substituted graphene. Yu et al. used organic amine as the nitrogen source to produce nitrogen-doped graphene aerogel (N-GA) by hydrothermal synthesis. Resulting devices had a high power density of 205.0 kW kg^{-1} at 185.0 A g^{-1} (Figure 3d-h).⁵⁴ Liu et al. prepared hierarchical porous nitrogen-doped GA by carbonizing in the presence of chitosan (nitrogen-containing biopolymer derivative). The

ARTICLE

Journal Name

resulting supercapacitors had a specific capacitance of 197 F g^{-1} .⁵⁵ Kang et al. employed nitrogen plasma treatment to dope the

graphene basal planes to yield capacitances of 280 F g^{-1} (Figure 3a-c) with excellent cycle life (>200000 cycles).⁵¹

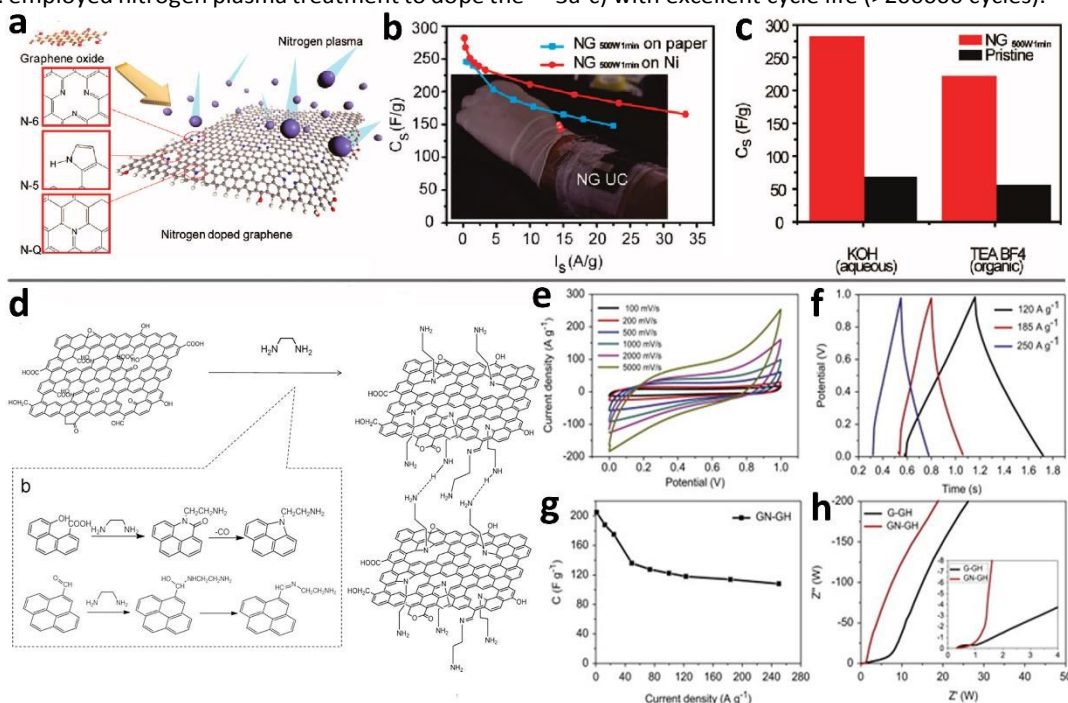


Figure 3. Plasma treatment to produce N-doped graphene⁵¹: (a) schematic illustration of N-doped moieties that can be found in graphene when treated with nitrogen plasma. (b) Gravimetric capacitances as a function of current density with inset photograph of an LED powered by a capacitor. (c) Comparison of specific capacitances between pristine and N-doped graphene (synthesized by hydrothermal method).⁵⁴ (d) Schematic illustration of N-doped graphene synthesis by a hydrothermal method. (e) CV curves as a function of scan rates. (f) Galvanostatic charge-discharge curves. (g) Specific capacitance as a function of current density. (h) Nyquist plots showing real and imaginary components of resistance.

High specific surface area can increase the effective contact area between the electrode materials and electrolyte to reduce the transfer distance for the electron charge and enhance the power density.^{56, 57} When increasing the BET, activation of graphene aerogel was a great way to increase the porous structure. Since KOH has a strong etching effect on carbon materials, Ruffo et al. activated graphene with KOH to increase the porosity. The BET of etched graphene reached $3100 \text{ m}^2 \text{ g}^{-1}$, which exceed the theoretical BET of graphene ($2800 \text{ m}^2 \text{ g}^{-1}$). When incorporated into a modified graphene supercapacitor, energy densities as high as 70 Wh kg^{-1} were observed.⁵⁸ Lei et al. reported the activation of graphene aerogel with phosphoric acid to realize a specific capacitance of 204 F g^{-1} (Figure 4).⁵⁹ CVD-growth could produce few-layer graphene with no cracks or collapses. This contributed to higher BETs and conductivities than aerogels prepared by the oxidation-reduction method.^{17, 60} Zhang et al. deposited graphene aerogel on Ni foam with a BET of $463 \text{ m}^2 \text{ g}^{-1}$ and conductivity of 71.4 S m^{-1} affording a specific capacitance of 366 F at 2 A g^{-1} .⁶¹ Bando et al. reported the preparation of high-power/high-energy GA-based supercapacitors through a substrate-free sugar blowing process to significantly increase the BET of the electrode.³⁵

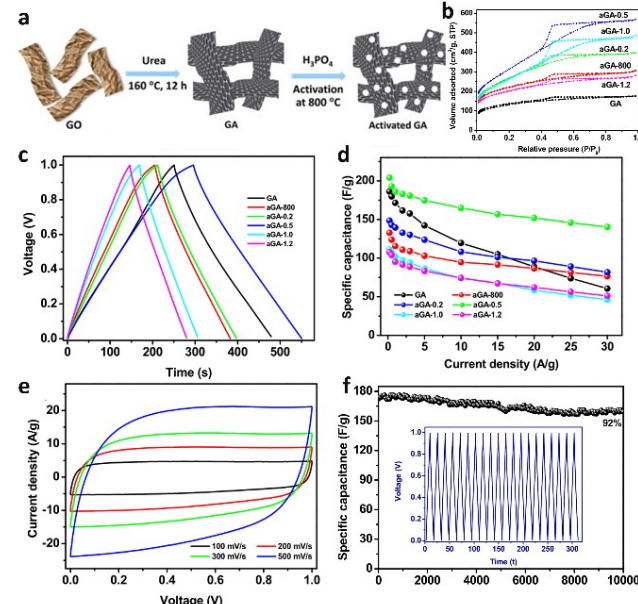


Figure 4. (a) Schematic for synthesis and acid activation of GA and (b) SEM of activated GA. (c) N_2 adsorption-desorption isotherm. (d) Charge-discharge curves showing high stability up to 10,000 cycles. (e) Cycling performance of various graphene aerogel-based supercapacitors. (f) Specific capacitance of activated GA supercapacitors using different concentrations of H_3PO_4 .⁵⁹

In addition to having a high BET, the size and distribution of pores in graphene aerogels are also key factors dictating overall performance. Pores in graphene aerogels are divided into three categories: macropores (greater than 50 nm), mesopores (2–50 nm), and micropores (less than 2 nm). Each pore size plays specific roles within the cycling supercapacitor device. Macropores store electrolyte ions, mesopores offer electrolyte ion transport, and micropores enable charge accommodation.^{62, 63} During activation, macropores are formed by the corrugations of the closely packed graphene layers, while micro and mesopores are directly formed by activation (i.e., etching). Song et al. prepared well-developed porous structures by chemical activation using K_2CO_3 with excellent capacitance properties (300 F g^{-1}).⁶⁴ Park et al. used CO_2 to activate graphene

aerogels creating hierarchical trimodal porous graphene aerogels with a capacitance of 278.5 F g^{-1} ⁶⁵ and good cycle stability.⁶⁵ Feng et al. described another way to produce macro and mesopores by adding tetraethoxysilane silica source (TEOS) and annealing at 800°C . The resulting 3D graphene aerogel- SiO_2 had large capacitances (226 F g^{-1}), high charging rates, and good cycle stability (Figure 5 a-d).⁶⁶ Recently, Li et al. combined graphene oxide (GO) and graphene nanoplatelet in an inks for 3D printing of periodic macroporous graphene aerogels for supercapacitor applications. The supercapacitors using these GAs delivered a maximum power density of 4079.9 W kg^{-1} at 0.26 Wh kg^{-1} (Figure 5e-i).⁶⁷

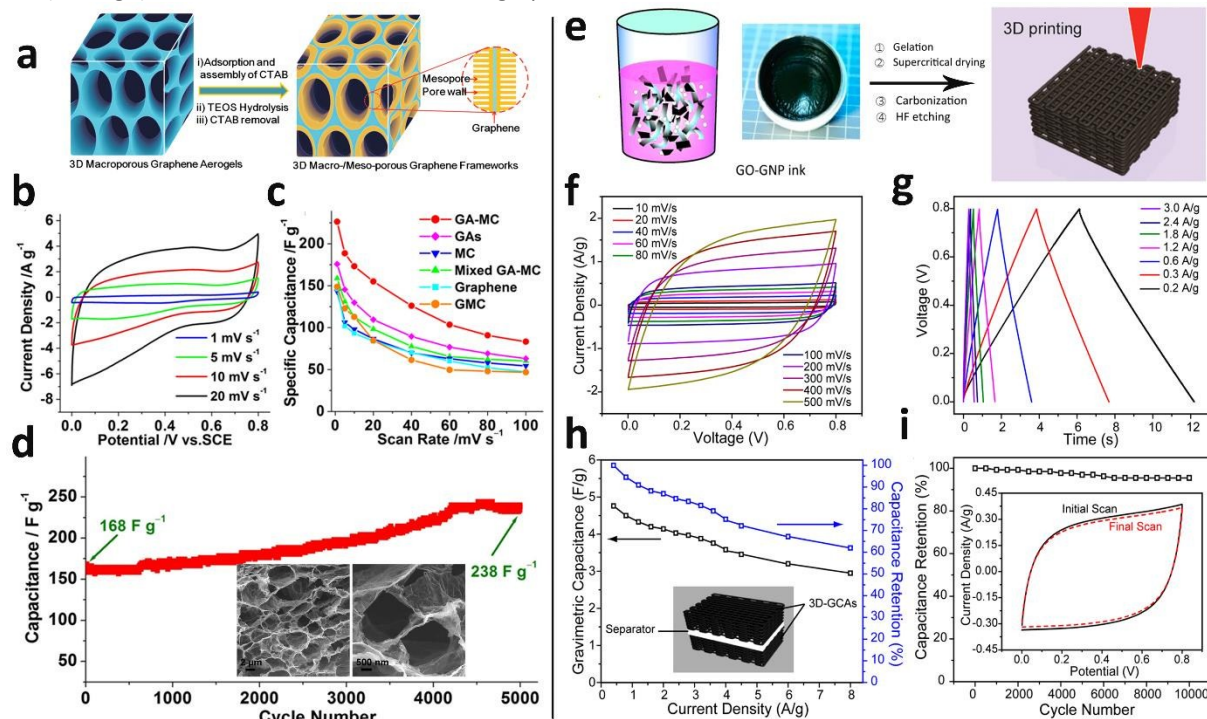
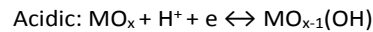


Figure 5. Macro and mesoporous graphene aerogels.⁶⁶ (a) Schematic illustration of synthesis process and hierarchical pore structure formation (TEOS method). (b) CV curves collected in $1 \text{ M H}_2\text{SO}_4$ over different scan rates. (c) Specific capacitance for GA-mesoporous carbon (MC), GAs, MC, mixed GA-MC, 2D graphene mesoporous carbon, and graphene powder electrodes. (d) Cycling stability at 2 A g^{-1} in $1 \text{ M H}_2\text{SO}_4$ electrolyte with inset showing periodic macroporous graphene aerogels.⁶⁷ (e) Schematic illustration of fabrication approach. (f) CVs measured for different scan rates in 3 M KOH . (g) Charge-discharge profiles. (h) Gravimetric capacitance and capacitance retention. (i) Cycling performance at a scanning rate of 200 mV s^{-1} .

3.1.2 Pseudo-capacitors

Although double-layer capacitors have excellent stability due to a largely physical process dominating the charge/discharge processes, their capacitance remains relatively low. Pseudo-capacitors rely on highly reversible electrochemical adsorption/desorption processes or oxidation-reduction reactions for storing energy. These reactions lead to deposition of materials onto the various surfaces and sub-surfaces.^{68, 69} Pseudo-capacitors are usually asymmetric supercapacitors whose cathodes are typically carbon materials and anodes are metal oxides (MOs) or conducting polymers. The supercapacitor energy storage type can be classified into three groups: highly reversible chemical adsorption-desorption (such as oxygen

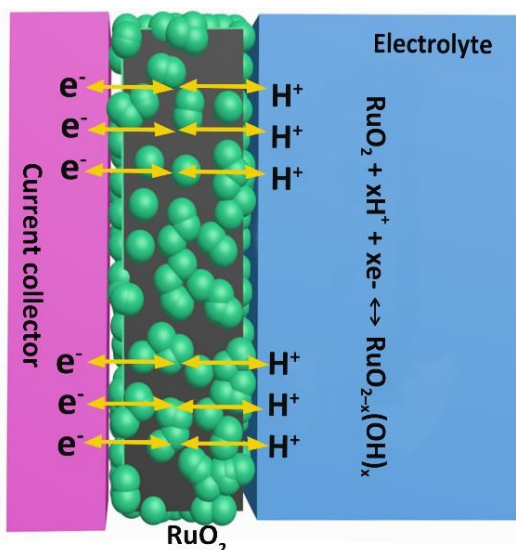
adsorption onto Pt or Au), fast reversible redox reactions (such as transition metal oxides or hydroxides), and reversible electrochemical doping and de-doping (such as polyaniline or polypyrrole). The energy storage mechanism in metal oxide-based pseudo-capacitors in acidic (Scheme 2) or alkaline solution can be considered a rapid and reversible electron transfer process accompanied by an adsorption of protons onto the metal oxide surfaces according to the following equations:



ARTICLE

Journal Name

When organic electrolytes are used to go increase the operating voltage window, the charge storage mechanism is based on electrolyte cations C^+ (K^+ , Na^+) and proton incorporation on the surface.



Scheme 2. Schematic diagram of pseudocapacitors, displaying the pseudo-capacitive behaviour of RuO_2 in acidic solution where oxidation states of Ru range from (II) to (IV).

GAs composed of hexagonally bonded sp^2 C atoms have complementary electrochemical windows, a 3D network structure with high surface area, and large pores that prevent the aggregation of graphene layers while also facilitating ion diffusion for enhanced rate performance (Figure 6).⁷⁰ Duan et al. successfully fabricated pseudo-capacitors with 3D graphene aerogel as the anode and aligned MnO_2 on nickel foam as the cathode. The device exhibited a broad potential window of 0–2.0 V and a high energy density of 23.2 Wh kg^{-1} with 83.4% retention after 5000 cycles.⁷¹ Li et al. also manufactured high energy density pseudo-capacitors with a nickel oxide cathode and a reduced graphene aerogel anode.⁷² The device had a capacitance of 248 mF cm^{-2} and a high energy density of 39.9 W h kg^{-1} at a current density of 1 mA cm^{-2} . These electrodes directly grew on metals (or metal oxides) without the need for polymer binders. This likely contributed to the good electrochemical performance because most of polymer binders are electrochemically inactive.

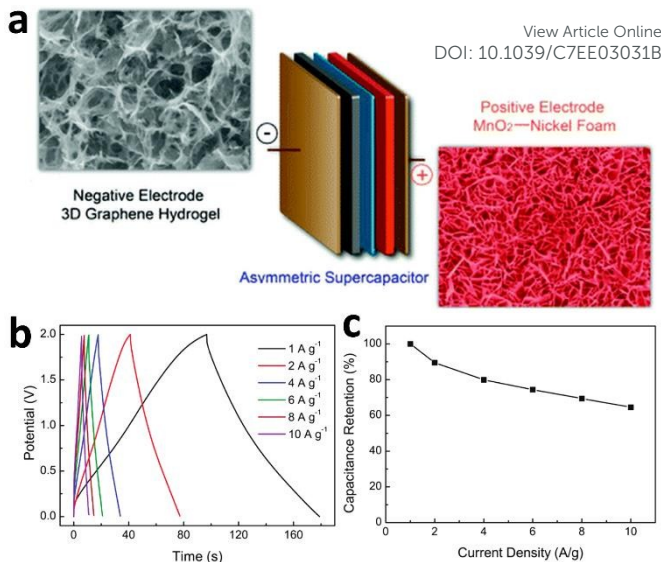


Figure 6. Pseudo-capacitor with graphene aerogel cathode and MnO_2 -nickel foam anode⁷¹: (a) Illustration of the layered construction of an asymmetric supercapacitor. (b) Galvanostatic charge-discharge curves at different current densities. (c) Capacitance retention ratio as a function of discharge current densities.

Transitional metal oxides or hydroxides have intriguing electronic, electrochemical, and electrocatalytic properties which can be applied in pseudo-capacitor reversible redox reactions to enable higher theoretical specific capacitances. However, high costs, limited stock, low electrical conductivity and cycle stability restrict the development of metal oxide supercapacitors. Incorporating metal oxides and hydroxides into conductive graphene aerogel networks can enhance the electrical conductivity, charge transfer, and structure stability.⁷³⁻⁷⁶ Chen et al. synthesized graphene aerogels via CVD growth and then incorporated cobalt oxide nanowires to form a composite for supercapacitors. The calculated specific capacitances were found to be 768 , 618 , 552 , and 456 F g^{-1} at 10 , 15 , 20 , and 30 A g^{-1} , respectively.⁷⁷ Jun et al. fabricated graphene/ Co(OH)_2 aerogels to improve the specific capacitances ($\sim 1139 \text{ F g}^{-1}$) and deliver higher energy densities ($\sim 13.9 \text{ Wh kg}^{-1}$) and power densities ($\sim 18 \text{ kW kg}^{-1}$) (Figure 7a-e).⁷⁸ Binary metal oxide electrodes perform better than single-component electrodes due to their more accessible oxidation states and higher electrical conductivity.⁷⁹ Xu et al. combined CoMoO_4 and 3D graphene networks to produce super long-life pseudo-capacitors providing a high specific capacitance of 2098 F g^{-1} at 5 A g^{-1} (Figure 7f-g).⁸⁰ The nano-honeycomb structure possesses a close-packed geometry that complements light weight and elastic materials.



ARTICLE

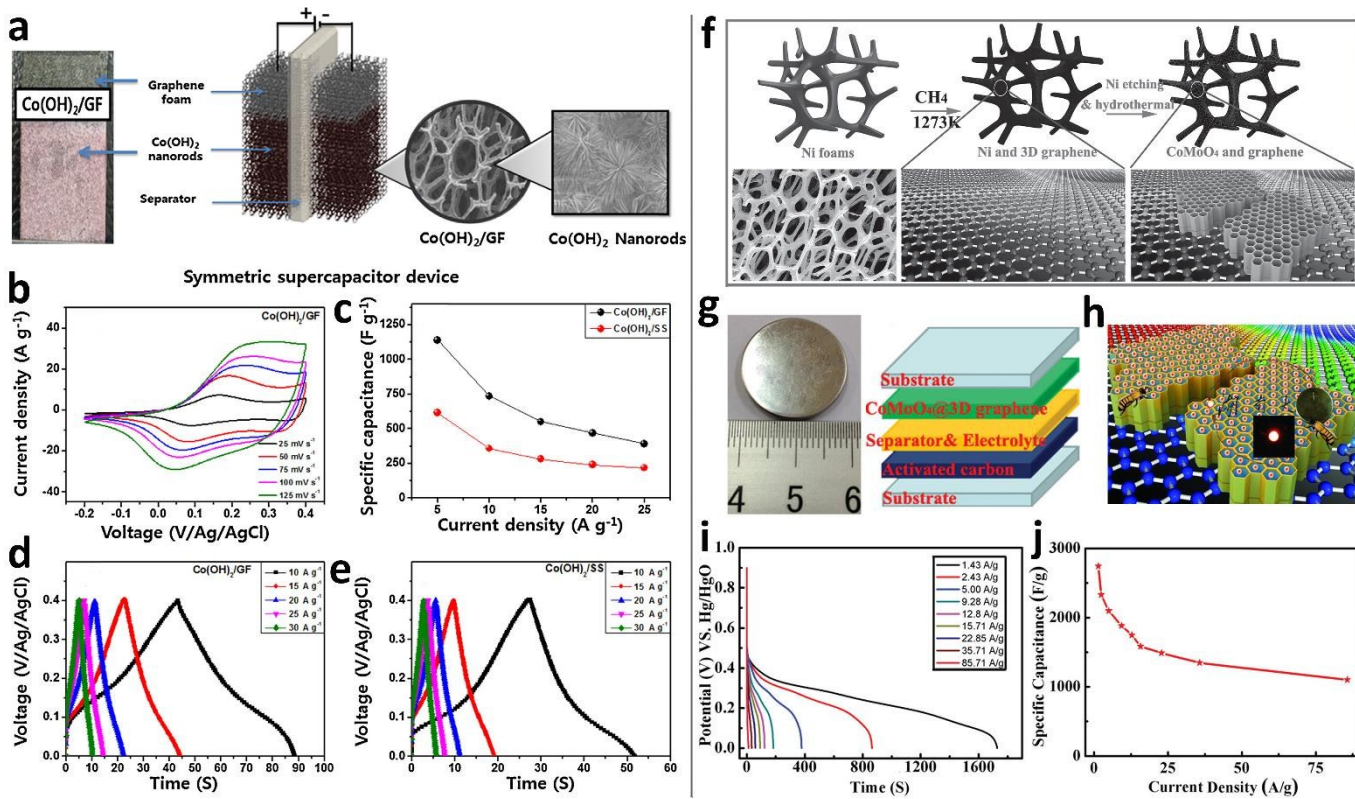


Figure 7. (a) Schematic illustration of a symmetric device. (b) CV curves at different scan rates. (c) Specific capacitance under different current densities. Charge-discharge curves using (d) Co(OH)_2 /graphene foam (GF) and (e) Co(OH)_2 /stainless steel (SS) electrodes.⁷⁸ (f) Synthesis procedure for honeycomb structure. (g) Schematic illustration of layered configuration. (h) Cartoon showing two supercapacitors that can light up an LED indicator. (i) Charge-discharge voltage profiles. (j) Specific capacitances with a GA/ CoMoO_4 electrode.⁸⁰

Conducting polymers are important active materials for supercapacitors due to their synthetic flexibility and variety, low cost, stability and high redox pseudocapacitance.^{42, 81-83} However, they also have several disadvantages such as mediocre conductivity and poor cycling stability due to swelling and shrinkage during the doping-dedoping process. Qu et al. fabricated polypyrrole/graphene aerogel composites to overcome these shortcomings. These highly compression-tolerant devices showed volumetric capacitances of 14 F cm^{-3} for uncompressed polypyrrole/GA which doubled to 28 F cm^{-3} when compressed by 50% (Figure 8).⁸⁴ This indicated no performance loss as a function of compression. These devices display high specific capacitances without obvious variation while compressive loads and unloads exerted. The development of strain-tolerant polymer/GA network composites for supercapacitors such as these will enable the development of next generation advanced supercapacitors that are tough. Polyaniline hybrids are an alternative storage material

amenable to large energy capture. Xiao et al. produced GA/polyaniline flexible all-solid-state supercapacitor hybrids that provided fast ionic conducting channels with a gravimetric energy density of 24.02 Wh kg^{-1} at a power density of 400.33 W kg^{-1} .⁸⁵ The protonated nitrogen atoms of polyaniline could bind to metal ions forming binary metal oxide/polymer complexes. These binary nano-hybrid structures have good electrochemical properties that can effectively increase the total capacitance.^{75, 86} Lu et al. fabricated GA/Polyaniline/ Co_3O_4 composites by hydrothermal synthesis. These ternary composites possessed large specific capacitances of 1247 F g^{-1} at 1 A g^{-1} and high cycle stability.⁸⁷ The specific capacitance, cycling, and voltage window of several GA compounds used in supercapacitors are summarized in Table 1.

ARTICLE

Journal Name

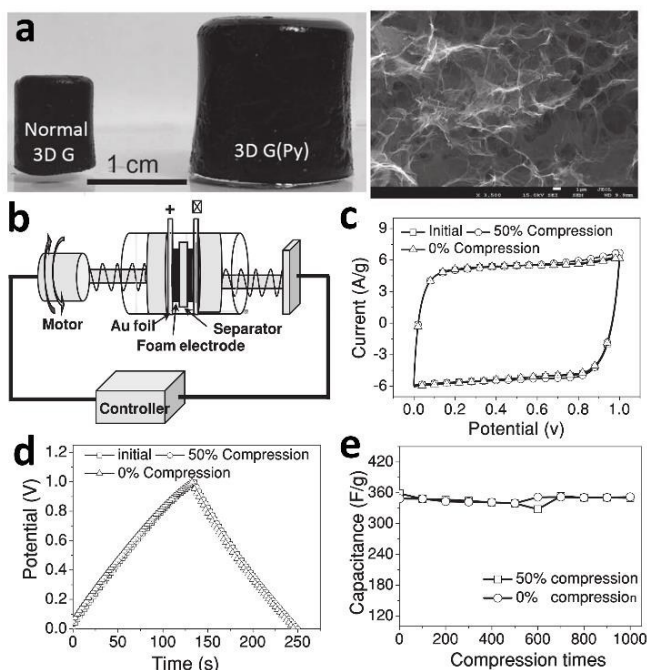
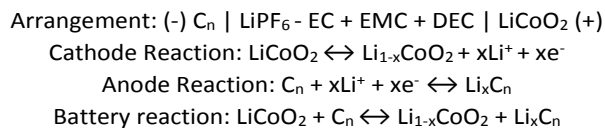


Figure 8. Characterization of strain-tolerant polypyrrole/GA network composites for supercapacitor applications: (a) Photograph and SEM image of polypyrrole/GA network composite. (b) Schematic illustration of polypyrrole/GA based supercapacitor device, (c) CVs of different compression states for one cycle, (d) Galvanostatic charge-discharge curves, and (e) cycling performance under 0% and 50% compression of GA/polypyrrole based supercapacitors devices.⁸⁴

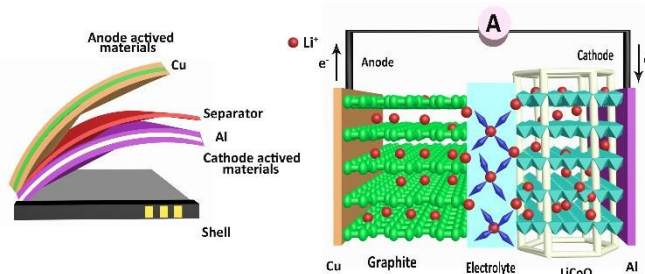
3.2 Lithium Batteries

Batteries are an essential energy storage technology which has seen a significant increase in energy density requirements as more powerful mobile devices and electric cars are developed. In contrast to other battery types (Ni-Cd, lead-acid, Ni-MH), lithium ion batteries possess high energy densities, long cycle life, no memory effect, and no self-discharge. Studies of lithium ion batteries began in the 1960s when the lithium anode was being developed. However, lithium ion batteries generated dendritic arms which can lead to shorts over time. To address this major safety concern, Armond et al. fabricated “rocking-chair batteries” that employed lithium-ion intercalated compounds, $\text{Li}_x\text{A}_y\text{B}_z$, as the anode and octahedral TiS_2 as the cathode in 1980. Next, SONY introduced commercial Li-batteries with carbonaceous anode materials and LiCoO_2 as the cathode. Lithium batteries have since found widespread use in phones, laptops, cameras, and electric vehicles due to their high power and energy densities. They are generally composed of a cathode, anode and electrolyte. Differing from pseudo-capacitors whose faradaic reaction occurs on the surface, the lithium ions in batteries can insert and diffuse into the solid phase of the electrode contributing to higher energy densities. Specifically, the lithium ions reversibly embed into and out of the positive and negative electrodes during charging and discharging. Lithium ions migrate out of the cathode lattice material and embed in anode material forming lithium compounds. The lithium ions migrate from one electrode to the

other through an electrolyte (lithium salt dissolved in an organic solvent). Consider a battery setup with a graphite anode, LiCoO_2 cathode, and LiPF_6 (1.0 mol L⁻¹) dissolved in ethylene carbonate (EC), ethylmethyl carbonate (EMC), and diethyl carbonate (DEC) (1:1:1 volume ratio) electrolyte (Scheme 3):



When charging, lithium ions are removed (deintercalated) from the crystal lattice of LiCoO_2 together with a change in Li oxidation states. The deintercalated lithium ions are transported by the non-aqueous electrolyte to the negative electrode (graphite) with electron capture and transfer to the external circuit through the anode. Lastly, the lithium ions are reduced to metallic lithium and held in between the graphite layers. The process is reversed during the discharge process. The conclusions section should come in this section at the end of the article, before the acknowledgements.



Scheme 3. Structure and schematic diagram of Li-ion batteries (graphite anode, LiCoO_2 cathode, and LiPF_6 dissolved in EC:EMC:DEC as the electrolyte).

3.2.1 Graphene Aerogel-modified Cathodes in Lithium Ion Batteries

Cathode materials are an essential component contributing to the energy storage capacity of lithium ion batteries. There are several common cathode materials. The first group consists of layered oxide structures. First, layered oxides of the form LiMO_2 ($\text{M} = \text{Co}, \text{Ni}, \text{Mn}$) are composed of MO_2 layers with octahedral MO_6 edged lines providing 2D diffusion paths for lithium ions. Another typical layered oxide has the form Li-Ni-Co-Mn-O (such as $\text{LiNi}_{1/3}\text{Co}_{1/3}\text{Mn}_{1/3}\text{O}_2$). These ternary layered structures combine the rate capability of LiCoO_2 , the high power capacity of LiNiO_2 , and the structural stability of Mn^{4+} .⁸⁸ Another example is $x\text{LiMnO}_3(1-x)\text{-LiMnO}_2$. This lithium-rich layered oxide has two different metal oxide structures: LiMO_2 ($\text{R}3\text{m}$) and Li_2MO_3 ($\text{C}2/\text{m}$). The residual lithium ions occupy transition metal layers with higher power capacity at initial charge.⁸⁹ The second group consists of spinel oxide structures. LiMn_2O_4 has a 3D frameworks for lithium ions to easily diffuse in and out of the structure. This material also has better safety performance. $\text{LiNi}_{0.5}\text{Mn}_{1.5}\text{O}_4$ is a Ni-doped spinel structure with Ni partially replacing Mn. This material has a higher rate capability and cycle stability than LiMn_2O_4 .⁹⁰ The third group consists of poly-

anionic compounds. LiFePO₄ (LFP) has a period structure that is thermodynamically stable, environment friendly and inexpensive. The strong covalent O-P and O-Fe bonds afford a highly stable and safe battery material.⁹¹

LFP has attracted increasing interests as a cathode material due to its several attractive properties including relatively high capacity, good stability, low cost, and environmental friendliness.^{92, 93} However, poor electrical conductivity and low Li-ion diffusivity have plagued its development. Designing 3D porous networks for the electrode material is an efficient way to create ion pathways throughout the electrode and improve electrical conductivity.⁹⁴ Zhao et al. combined N-doped graphene aerogels with LFP. This shortens the lithium ion diffusion length in LFP crystals and provides new and rapid pathways for lithium ion transport (Figure 9a-c). A cathode composed of LFP modified by 3D graphene displayed high rate capabilities (78 mAh g⁻¹ at 100°C) and excellent cycle stability.⁹⁵ Due to a theoretical storage 5-10 times that of lithium ion batteries, lithium-oxygen (Li-O₂) batteries are another promising lithium battery technology relying on porous carbon materials covered with gaseous O₂ as the cathode and lithium metal as the anode.^{96, 97} However, O₂ can easily oxidize Li⁺ to form insoluble Li₂O or Li₂O₂ during the charge-discharge process. This can lead to blocked oxygen pathways and reduced

performance.⁹⁸ The large pore volume of the added graphene aerogel is key to reducing the formation of pathway-blocking insoluble lithium peroxide and lithium oxide for prolonged battery life.⁹⁹ Zhang et al. prepared porous graphene aerogel/O₂ cathodes for Li-O₂ batteries. The batteries reached capacities of 11060 mA h g⁻¹ at 0.2 mA cm⁻² (280 mA g⁻¹) and 2020 mA h g⁻¹ at 2 mA cm⁻² (Figure 9d).¹⁰⁰ Owing to their multi-electron chemical reactions, lithium-sulphur (Li-S) based batteries have attracted much attention due to theoretical specific capacities 5 times and energy densities 2-3 times that of commercial lithium ion batteries.^{101, 102} However, the applicability of Li-S batteries remains limited due to poor conductivity and structural damage incurred during the charge-discharge processes.^{103, 104} Capitalizing on the conductivity and porosity of the graphene aerogel 3D network, Ren et al. constructed Li-S batteries with high sulphur loading (14.36 mg cm⁻² and total sulphur content of 89.4 wt.%) on GA. The device had a capacitance of 1000 mA h g⁻¹ (Figure 9e).¹⁰⁵ Selenium, another chalcogen element, has also been considered for use in lithium ion batteries but is limited by its low conductivity and high volume expansion.^{106, 107} He et al. fabricated tellurium nanowire/3D rGO for free-standing and binder-free Li-Te battery cathodes that showed a high initial capacitance of 2611 mA h cm⁻³ with 88% retention after 200 cycles.¹⁰⁸

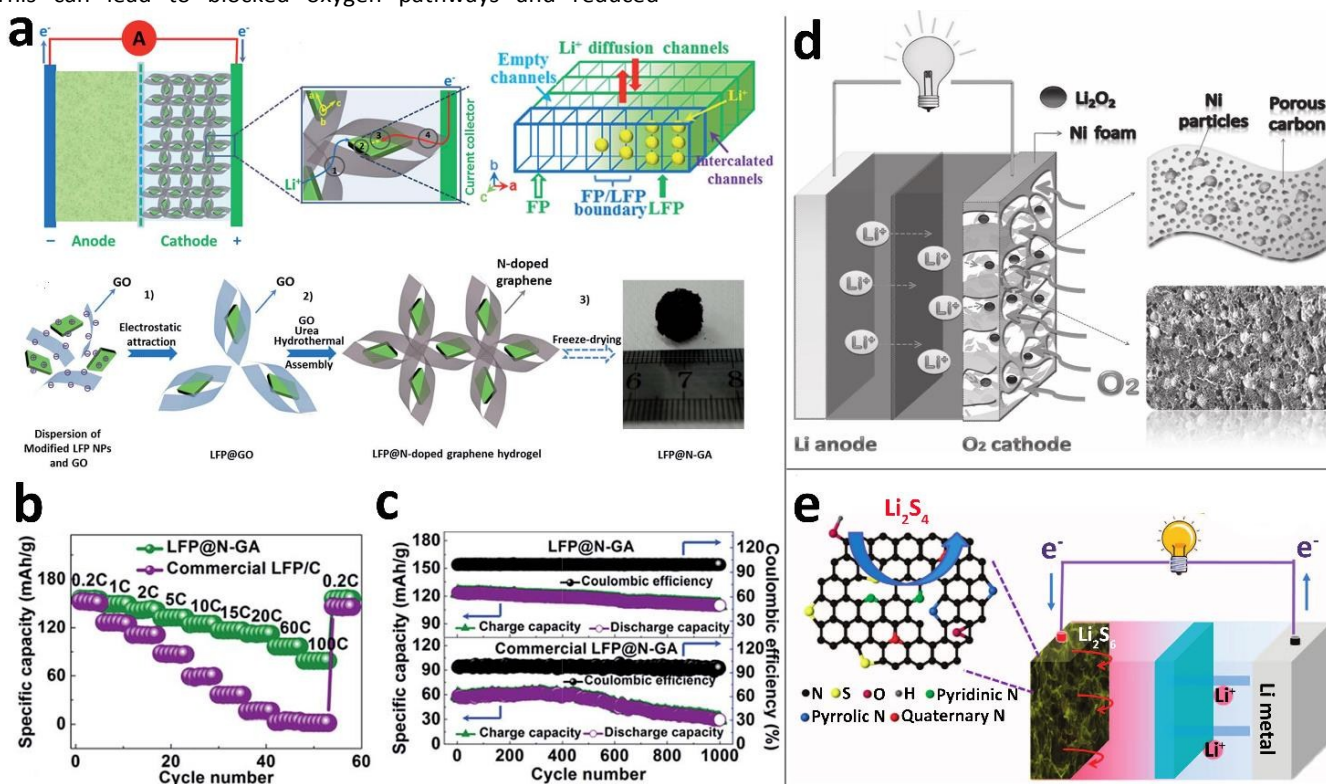


Figure 9. (a) Schematic illustration of LFP cathode structure showing the lithium ion diffusion pathways and synthesis approach. (b) Rate-dependent and (c) stability cycling performance of a lithium ion battery with N-GA/LiFePO₄ cathode.⁹⁵ (d) Schematic illustration of a porous graphene oxide cathode for a Li-O₂ battery enabling oxygen diffusion deep into the structure.¹⁰⁰ (e) Schematic illustration of a nitrogen and sulphur codoped graphene aerogel cathode for use in a Li-S battery.¹⁰⁹

ARTICLE

Journal Name

3.2.2 Modified Anodes

Despite the varied work in cathode materials design, more effort has been devoted to designing anode materials with large reversible specific capacity. There are several common anode materials currently being investigated. The first is carbon-based anode materials with graphite being the most popular due to its low potential, long cycle stability, high conductivity and low cost.^{110, 111} The second group is transition metal oxides grouped based on how lithium is incorporated into their structure. The first group includes MoO_2 , WO_2 , Fe_2O_3 , TiO_2 and Nb_2O_5 . In these metal oxides the lithium ion directly embeds within the structure. Another group of metal oxides have the form M_xO_y ($\text{M} = \text{Co, Ni, Cu, Fe}$). In these structures, Li_2O is produced when the ions are incorporated.¹¹²⁻¹¹⁴ The third groups is metal alloy anode materials. Representative materials include Si, Ge, and Sn which undergo alloying and dealloying with lithium during charging and discharging.^{115, 116}

Nanosscopic metal oxides (nano-MOs) are ideal anode materials for lithium ion batteries due to their several advantages.¹¹⁷ However, most nano-MOs are semiconductors with inherently poor electric conductivity restricting their performance in lithium ion storage.¹¹⁸ One approach to address the limitations of nanoscale metal oxides is to wrap them with conducting graphene sheets to produce a 3D network material with improved overall conductivity and improved accommodation to volume changes during charging and discharging.¹¹⁹⁻¹²¹ Feng et al. fabricated an interconnected macroporous 3D Fe_3O_4 /graphene aerogel. The device showed a high reversible capacity of 372 mA h g⁻¹ at high rate of 5000 mA g⁻¹ and 995 mA h g⁻¹ after 50 cycles at 100 mA g⁻¹.¹²² Similarly, a TiO_2 /graphene aerogel displayed an excellent capacity of 200 mA h g⁻¹ at 0.59 C after 50 cycles and a capacity of 99 mA h g⁻¹ at 5000 mA g⁻¹ (Figure 11a-e),¹²³ Wrapped Bi_2O_3 /graphene aerogel produced a large capacitance of 417 mA h g⁻¹ over 100 cycles at 200 mA g⁻¹ and 273 mA h g⁻¹ at 10000 mA g⁻¹.¹²⁴

Other MOs (M_xO_y ; $\text{M} = \text{Co, Ni, Cu, Fe}$) have also been incorporated into graphene aerogels for anode applications. Kim et al. demonstrated enhanced electron and ion transport for improved cycle stability in a Co_3O_4 /graphene aerogel anode showed corresponding specific capacities of 1001, 900 and 798 mA h g⁻¹ at 0.2, 0.5 and 1.0 A g⁻¹ (Figure 11f).¹²⁵ Fe_3O_4 /GA fabricated by Müllen et al. exhibited a capacity of 63 mA h g⁻¹ at 4800 mA g⁻¹ and cycling performance of 1059 mA h g⁻¹ over 150 cycles at 93 mA g⁻¹.¹²⁶

The range of performance values for batteries are also being pushed to higher levels. In general, lithium ion batteries tend to have high energy densities and low power densities. Recently, Duan et al. designed a 3D holey-graphene oxide/ Nb_2O_5 anode (Figure 10) with both a high energy density and power density at higher mass loadings.¹²⁷ They systematically tailored the graphene aerogel porosity to facilitate rapid ion transport and minimize diffusion limitations throughout the structure.

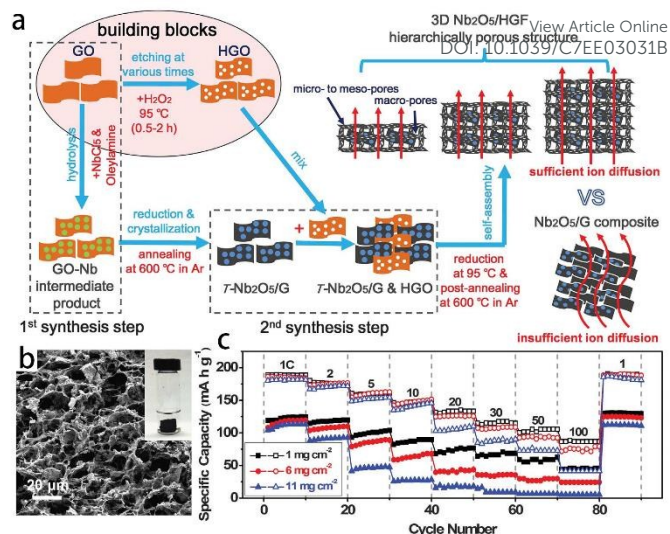


Figure 10. (a) Illustration of the two-step fabrication of holey graphene oxide HGO/ Nb_2O_5 . (b) Cross-sectional SEM image of free-standing composite of HGO/ Nb_2O_5 with inset showing bulk appearance. (c) Comparison of the rate performance of the open network (with ion channels) $\text{Nb}_2\text{O}_5/\text{HGO}$ and dense (without ion channels) $\text{Nb}_2\text{O}_5/\text{G}$ electrodes at different mass loadings.¹²⁷

Earth abundant alloys of Si, Sn, Ge and relevant oxides possess high reversible capacities ranging from 783 mA h g⁻¹ (SnO_2) to 4200 mA h g⁻¹ (Si) have attracted much attention for use in lithium ion batteries.¹²⁸⁻¹³⁰ Researchers have investigated the working mechanism of such materials for anode applications. For example, it was found that lithium ions can break Si-Si bonds to form isolated Si clusters. The lithium ions then embed in the clusters to locally form Li-Si alloys ($\text{Li}_{15}\text{Si}_4$).¹³¹ However, the migration of a large number of lithium ions into and out of the structure leads to large volume changes and subsequent pulverization of the anode material ultimately shortening the batter lifetime.^{132, 133} Graphene, owing to its excellent electrical conductivity, flexibility and high BET, make it a suitable reinforcement material for enhancing the coulombic efficiency and rate capability of various incorporated alloys.¹³⁴ Similarly, 3D networks maintain structural stability and transport electrons and ions between the GA walls and alloy.^{135, 136} Zheng et al. synthesized amorphous SiO_2 /graphene aerogel anodes that showed reversible capacities of 300 mA h g⁻¹ at 500 mA g⁻¹ and stable cycling performance.¹³⁷ He et al. prepared Sn/3D network graphene which showed a capacitance of 1022 mA h g⁻¹ at 200 mA g⁻¹, 459 mA h g⁻¹ at 5000 mA g⁻¹ with 96.3% performance retention after 1000 cycles (Figure 11g).¹³⁸ The role, cyclability, and rate capability of various GA compound materials for lithium batteries are listed on Table 2.

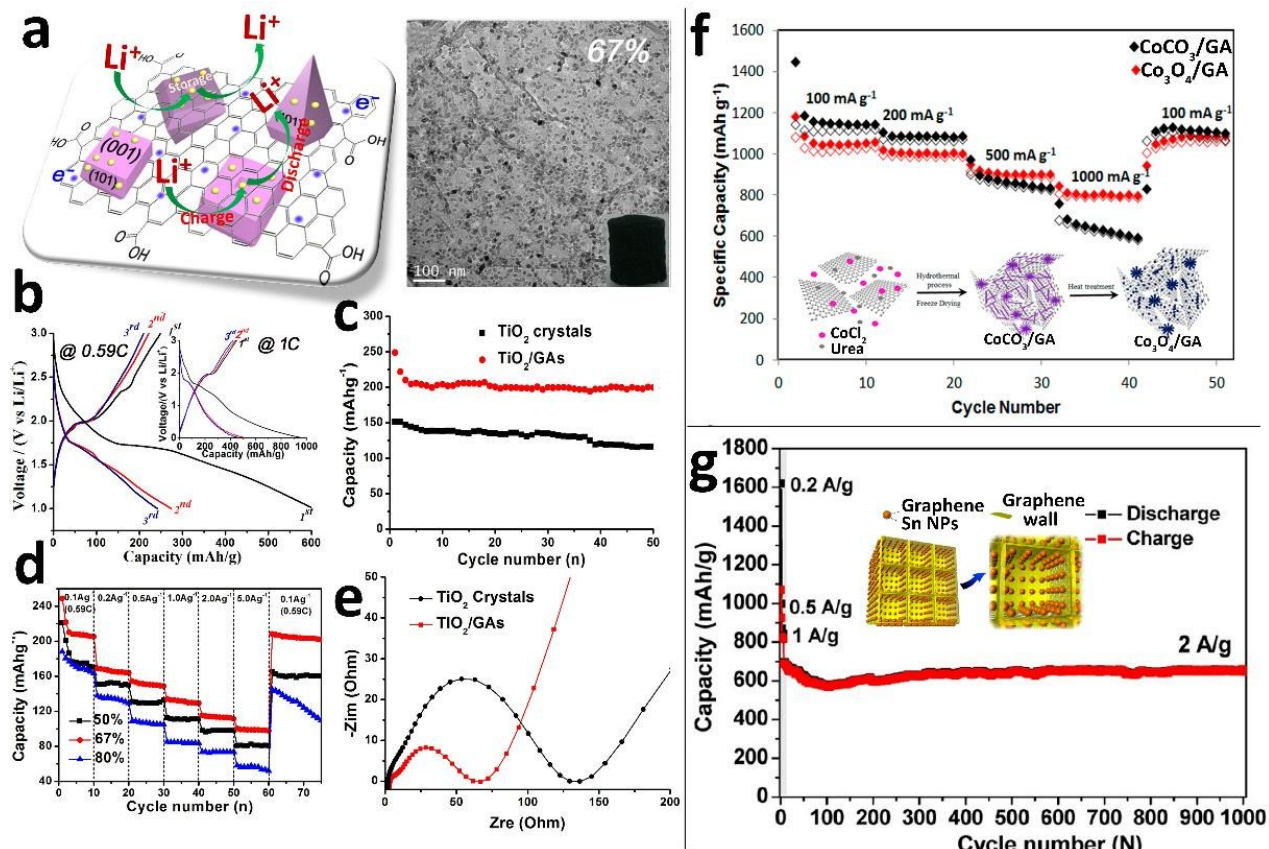


Figure 11. (a) Schematic illustration of the electrochemical reaction path taken by lithium ions during charging and discharging with TEM image of the TiO₂/graphene aerogel composite. (b) Galvanostatic charge–discharge profiles of the electrode. (c) Cycling performance with different current densities from 0.1 to 5.0 A g⁻¹. (d) Cycling performance at different current densities. (e) Nyquist plots of TiO₂/GA;¹²³ (f) Rate performance and synthesis process for CoCO₃/GA and Co₃O₄/GA;¹²⁵ (g) Schematic illustration of structure and cycle performance of Sn@graphene.¹³⁸

3.2.3 Other Batteries

Lithium ion batteries have been successfully commercialized into a global portable energy storage system over the past several decades. However, the increasing demand for lithium ion batteries is met with increasingly scarce natural availability of lithium sources and consequently higher costs (\$5000 per ton of lithium). In anticipation of limited supply and increasing costs of lithium-based energy storage, the development of other battery types based on sodium, aluminium, and magnesium have attracted more attention due to their natural abundance and significantly lower costs.^{139–141} Specifically, Na, Mg and Al based materials have been developed for use in cathodes. Whereas carbon materials, with chemical stability, low

environmental impact, low cost, and high conductivity, are promising anode materials. The porous morphology and pore diameter of carbon-based anodes accounts for the high electrochemical performance and large ion storage potential. Dai et al. prepared 3D N-GA with a high nitrogen (6.8 at%) content and capacitance of 1057.1 mAh g⁻¹ at 200 mA g⁻¹ and 244.7 mAh g⁻¹ at 4000 mA g⁻¹ (Figure 12a-f).¹⁴² 3D porous carbon networks and defects induced by heteroatom-doping were promising for anode materials. Yao et al. synthesized V₂O₅/GA as magnesium battery cathodes showing 330 mAh g⁻¹ (1000 mA g⁻¹) capacity over a wide working temperature range from -30.1°C to 55°C with long-cycle-life (80% retention after 200 cycles, Figure 12g-h).¹⁴³



ARTICLE

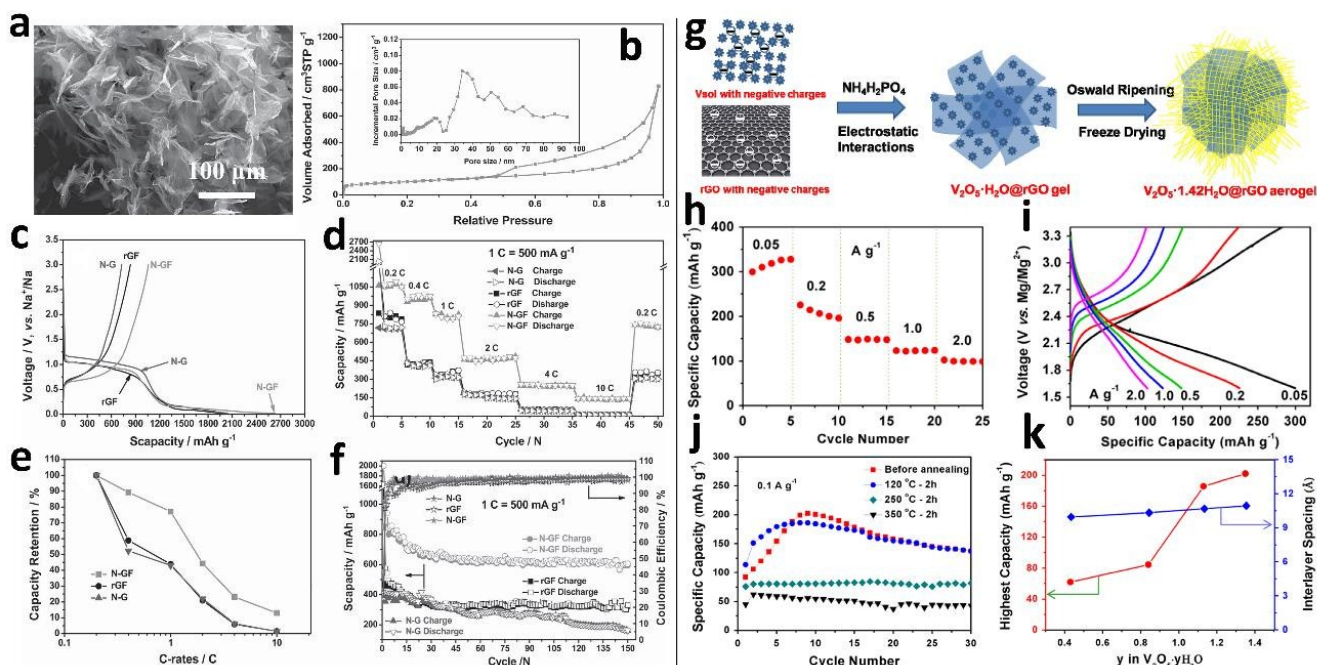


Figure 12. (a) SEM image, (b) nitrogen adsorption–desorption isotherm and pore size distribution curve, (c) initial charge–discharge curves at 0.2 C, (d) rate performance from 0.2 C to 10 C, (e) capacity retention , and (f) cycling performance of N-doped 3D graphene foam anode in a Na-ion battery.¹⁴² (g) Schematic illustration of V₂O₅-nH₂O/GA fabrication process, (h) rate performance, (i) charge–discharge profiles, (j) cycling performance of samples annealed at different temperatures, and (k) the effect of crystal water content on the capacity of GA/V₂O₅·nH₂O.¹⁴³

Hydrogen has been investigated as an alternative fuel source due to its low environmental impact, high efficiency, and abundance.^{144, 145} Compared to other hydrogen storage materials like metal alloys, COFs and MOFs, graphene-based materials can function over a wide range of conditions with excellent structural stability.^{146–148} Froudakis et al. fabricated new 3D network pillar graphene with tunable pore sizes. They utilized a multiscale theoretical approach to measure the H₂ storage (41 g L⁻¹) under ambient conditions (Figure 13a, b).¹⁴⁹ Jhi et al. developed a porous 3D graphene with dispersed Ca atoms anchored to the carbon centers of graphene forming chain-like structures. The total hydrogen storage capacity of this 3D Ca-graphene composite reached 5–6 wt % and hydrogen adsorption at the vertices of Ca chains exhibits the multipoles Coulomb and Kubas interactions.¹⁵⁰ In particular, high specific surface area and pores with diameters around 0.7 nm possess higher hydrogen adsorption. Zhu et al. synthesized graphene aerogels with acetone and trifluoroacetic acid to carbonize multifunctional aerogels to produce a high specific surface area and small pore diameters. Such structures with pore sizes of 0.72 nm showed unexpectedly high hydrogen adsorption.¹⁵¹

Thermal management has been a significant concern dictating progress in the electronics industry. Phase change materials (PCMs) have been widely applied in thermal management and energy storage for transition-edge sensors (TES).^{152–154} In addition to its superior electrical conductivity, graphene also possesses excellent thermal conductivity (~5000 W m⁻¹ K⁻¹) which makes it especially appropriate for thermal storage.^{155, 156} Thus 3D interconnected graphene aerogel networks can greatly reduce or eliminate thermal resistance in energy capture/storage devices.¹⁵⁷ Huang et al. combined graphene sheets and octadecanoic acid (OA) into a GA/OA hybrid material. The thermal energy generated (181.8 J g⁻¹) was stored in the GA/OA hybrid.¹⁵⁸ They further deposited porous graphene by CVD growth onto aluminium oxide with ceramic which has a latent heat of 186 J g⁻¹.¹⁵⁹ Feng et al. constructed core–shell GA for shape-stable PCMs showing a high encapsulation ratio of paraffin, excellent cycling performance and a latent heat of 213 J g⁻¹ (Figure 13c).¹⁶⁰

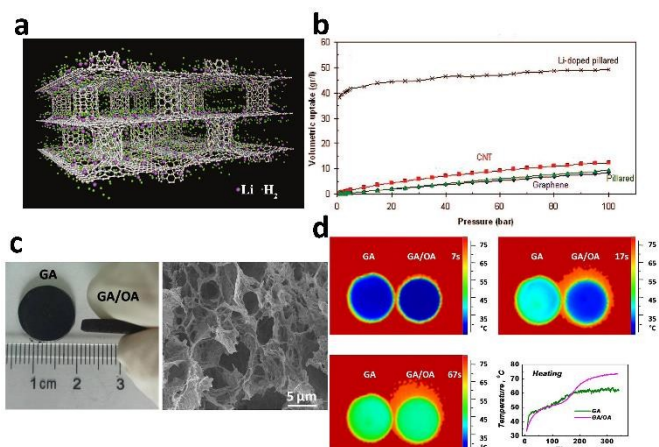
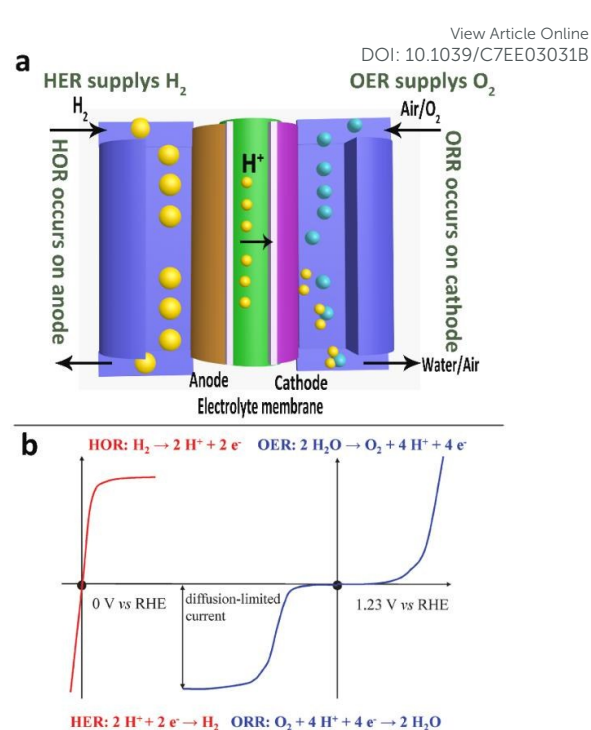
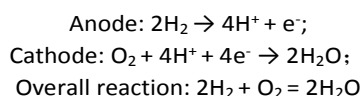


Figure 13. (a) Snapshot from Monte Carlo simulations of Li-doped graphene pillar structures for hydrogen storage. (b) Comparison of graphene, carbon nanotube, pillared graphene and Li-doped pillared graphene volumetric hydrogen uptake.¹⁴⁹ (c) Schematic illustration of the formation process of modified hydrothermal-graphene/paraffin (MH-GPn). (d) The measured latent heats and (e) images of different core-shell graphene aerogel composite formulations at different temperatures.¹⁵⁸

4. Mechanisms and Roles of Graphene Aerogels in Energy Conversion

Fuel cells and solar cells that directly convert chemical or solar energy into electrical power are a significant technology for harnessing renewable energy. Oxygen reduction reaction (ORR), oxygen evolution reaction (OER) and hydrogen evolution reaction (HER) are three electrochemical processes (Scheme 4b) that take place in metal-air batteries, regenerative fuel cells, and water splitting cells respectively.¹⁶¹

Fuel cells offer a convenient way to generate electricity with high efficiency, stability, and longevity; all three of which are essential for applications in portable electronic devices and electric cars.^{162, 163} Fuel cell systems directly transform chemical energy from fuel gas (such as hydrogen or methane) into electrical energy. Fuel cells can be classified into five different types according to the electrolyte used with each having specific ranges of operating temperature. The types include: (1) proton-exchange membrane fuel cells (PEMFC, 50–100°C), solid oxide fuel cells (SOFC, 500–1000°C), molten carbonate fuel cells (MCFC, 650–800°C), phosphoric acid fuel cells (PAFC, 160–210°C), and alkaline fuel cells (AFC, 60–100°C).^{164–167} The simplified mechanism behind proton exchange membrane fuel cells is highlighted in Scheme 4a. First, gaseous H₂ is broken into two protons (H⁺) by the anode catalyst. After passing through the proton exchange membrane the protons react with oxygen at the cathode to produce water. When an acidic electrolyte is utilized; the anode, cathode and overall reaction can be written as follows:



Scheme 4. (a) Schematic diagram of a fuel cell. (b) The polarization curves of key energy-related electrochemical reactions in fuel cells and their overall reaction equations.¹⁶¹

4.1 The Oxygen Reduction Reaction (ORR) and Oxygen Evolution Reaction (OER)

In the ORR oxygen reacts with both electrons and protons to form H₂O (4 electrons absorbed) or H₂O₂ (2 electrons absorbed). This reaction is essentially what occurs at the cathode of fuel cells and metal-air batteries. It is in many ways the biggest advantage of PEMFC as the only by-product is water. Platinum (Pt) and its alloys remain the most popular ORR catalysts. However, due to its scarcity and oftentimes prohibitive cost, the use of Pt has contributed to hindered large-scale development and commercialization of fuel cell systems.^{168, 169} Consequently, low-cost alternative catalysts such as earth-abundant metals (Fe, Co, etc.), metal oxides (Fe₂O₃, Fe₃O₄, Co₃O₄, MnO₂, etc.), and metal-free carbon-based materials have attracted much interest.^{170–173} Graphene aerogels or 3D network graphene have high BETs, fast electron-transfer kinetics, excellent mechanical strength, and porous structures providing sufficient contact and high stability for the ORR. Carbon materials doped by N, B, and P have shown improved ORR performance.^{174, 175} Chen et al. prepared N-Doped graphene metal-free catalyst with an ORR peak centred at -0.31 V with a current density of -2.9 mA cm⁻² and H₂O₂ yield below 14.7%,¹⁷⁶ while He et al. fabricated N and B-doped graphene which had a current density 6.2 mA cm⁻² and H₂O₂ yield less than 10% (Figure 14i, f).¹⁷⁷ Chen et al. created holey surface structures on N-GA to create more exposed active edge sites to further improve the catalytic performance of the metal-free catalyst for ORR.¹⁷⁸ Yi et al. incorporated carbon nanotubes (CNT) into a CNT/N-GA composite with a nano leaf-like network, and N-doped CNT containing 85% graphene

ARTICLE

Journal Name

aerogel (N-CNT@GNRs85-A) as a metal-free catalysts for ORR had a current density of 31.8 mA cm^{-2} and H_2O_2 yield below 5.5%.¹⁷⁹ Bagheri et al. developed a Co/N-doped GA glassy carbon electrode (Figure 14a-d) that showed excellent catalytic activity and stability for ORR in acid.¹⁸⁰ Müllen et al. prepared N-GA/Fe₃O₄ by a hydrothermal self-assembly process. This material displayed a more positive onset potential (-0.19 V) for ORR and a high current density (-2.56 mA cm^{-2}). Linear sweep voltammograms (LSV) measured at 10 mV s^{-1} in 0.1M KOH

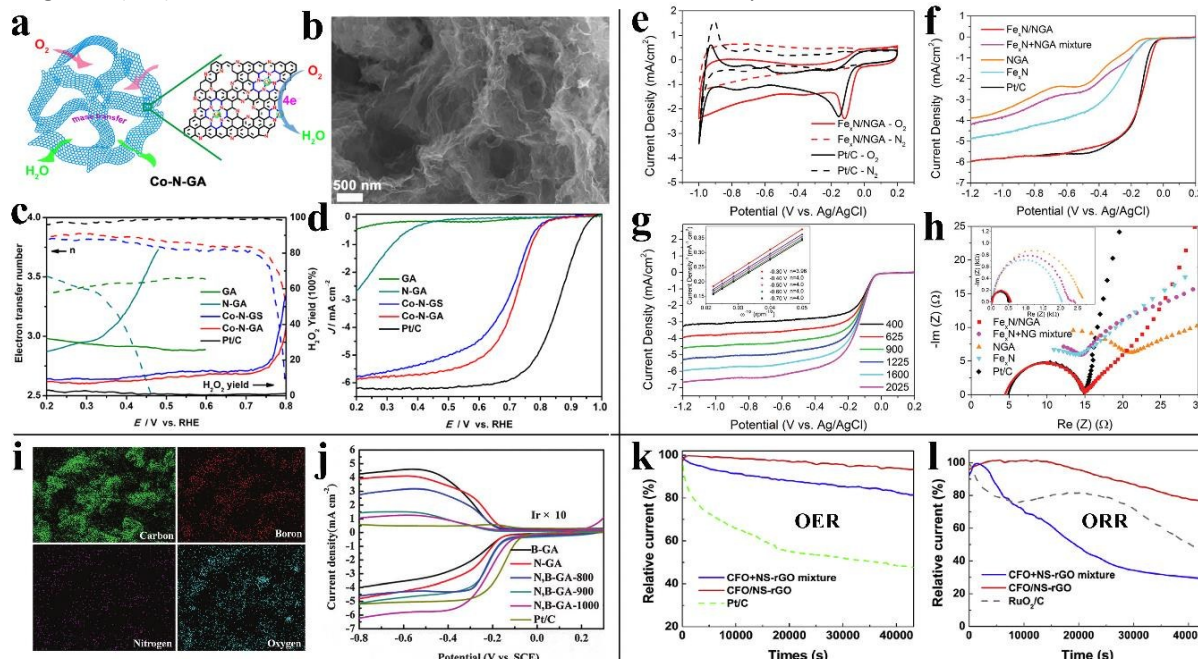
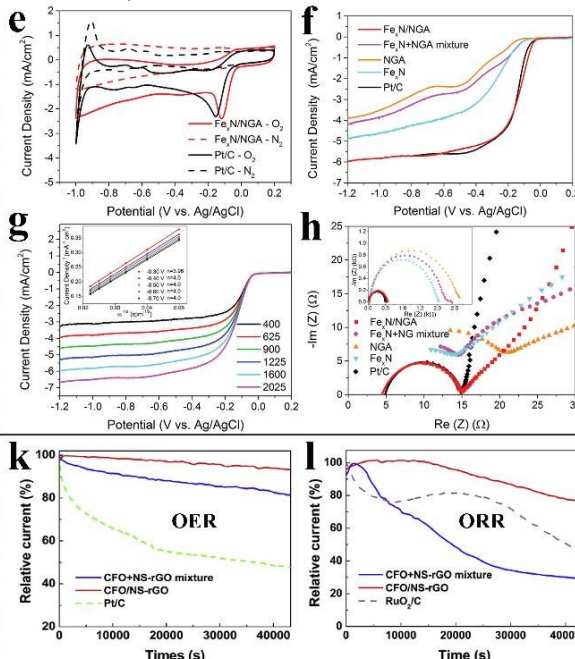


Figure 14. (a) Schematic illustration of ORR in graphene network composites. (b) SEM image of a metal and nonmetal co-doped graphene aerogel. (c) Rotating disk electrode (RRDE) polarization curves, (d) electron-transfer number and H_2O_2 yield of Co-N-GA for ORR.¹⁸⁰ (e) and (f) CV curves for various Fe-N co-doped graphene aerogel composites. (g) Current density curves and power density curves. (h) Electron impedance spectroscopy curves of $\text{Fe}_x\text{N}/\text{N-GA}$, $\text{Fe}_x\text{N}+\text{N-GA}$ mixture, N-GA, Fe_xN , and Pt/C.¹⁷⁶ (i) EDS chemical mapping of various composites. (j) Linear sweep voltammogram (LSV) curves of N, B-doped GA for OER.¹⁷⁷ Current-time chronoamperometric responses for OER (k) and ORR (l) of $\text{CoFe}_2\text{O}_4@\text{N,S-GA}$.

Fuel cells and metal-air batteries systems are both attractive energy storage technologies. The former requires optimization of the ORR whereas the latter requires an understanding of both OER and ORR which occur during charging and discharging respectively.¹⁸⁵⁻¹⁸⁷ Similar to the costs and scarcity of Pt catalysts for ORR, effective OER catalysts, such as RuO₂ and IrO₂, are relatively scarce and expensive.¹⁸⁸ Designing and synthesizing alternative catalysts with high activity, stability, and low-costs remains a challenge for both ORR and OER and thus a challenge in the commercialization of fuel cells and metal-air batteries. Considering that the two processes are essentially opposites, it is not surprising that the OER is associated with high potentials whereas the ORR is associated with low potentials. Yang et al. developed N/S-doped rGO 3D networks containing CoFe_2O_4 . This material exhibited a positive onset potential, peak potential (0.13 V and 0.28 V) and current density (3.79 mA cm^{-2}) for ORR and higher onset potential of 0.51 V and current density of 22.94 mA cm^{-2} for OER.¹⁸⁹ Chen et al. fabricated 3D hollow crumpled graphene–cobalt oxide that served as a high-performance bi-functional electrocatalyst with

showed a direct four-electron transfer pathway from -0.19 to -1.2 V for producing OH^- ions and an H_2O_2 yield of 30% at a potential of -0.4 V.²⁷ In addition, various metals and metal chalcogenide particles have been incorporated into 3D porous graphene including Pt/GA, CdS-P25/GA, Co/N-GA, and Fe-nitride/N-GA (Figure 14e-h).¹⁸¹⁻¹⁸⁴ As always, the graphene aerogel provides a high surface area and porosity while the nanoparticles offer more active sites for considerably enhanced ORR activity.



an OER lower overpotential of 0.34 V and ORR onset potential of (0.90 V) exhibiting a current density of 10 mA cm^{-2} with little attenuation (12%).¹⁹⁰ Most carbon catalysts reported are combined with noble metals (such as Pt) and metal oxides for OER and ORR. The incorporation of polymers into such catalysts was relatively new and unexplored until recently. Dai et al. designed a N, P co-doped polyaniline aerogel with graphene edges for bifunctional electrocatalysis.¹⁹¹ Simulations showed that N,P co-doping, graphene edge effects and the highly porous network contributed to a strong activity in both OER and ORR. Liu et al. further synthesized N-doped graphene with an interconnected 3D architecture (denoted by N-GRW).¹⁹² This interesting structure demonstrated a site-specific catalytic contribution to both OER and ORR. It was found that the electron-withdrawing pyridinic N section of N-GRW was responsible for catalyzing the OER, and the electron-donating quaternary N sites largely catalyzed the ORR (Figure 15e). Consequently, N-GRW served as an air cathode in Zn-air batteries exhibiting an open-circuit voltage of 1.46 V and a specific capacity of 873 mAh g^{-1} .

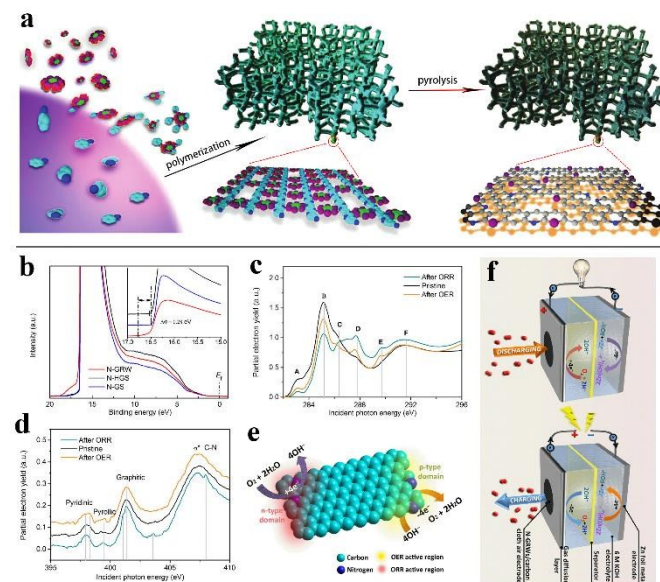


Figure 15. (a) Schematic illustration of the synthesis of metal-free polyaniline aerogel/graphene edge electrocatalyst for OER and ORR.¹⁹¹ (b) Ultraviolet photoelectron spectroscopy (UPS) spectra collected under He 1 α (21.2 eV) radiation. Carbon (c) and nitrogen (d) K-edge x-ray absorption near-edge structure (XANES) spectra. (e) Schematic diagram of ORR and OER taking place at the n- and p-type domains of the 3D N-graphene network.¹⁹²

4.2 The Hydrogen Evolution Reaction (HER) and CO₂ Reduction

Hydrogen is considered an ideal clean energy alternative to replace fossil fuels. The hydrogen evolution reaction (HER), in which hydrogen is generated from water splitting in fuel cells, is one of the most important methods for making hydrogen.^{161, 193}

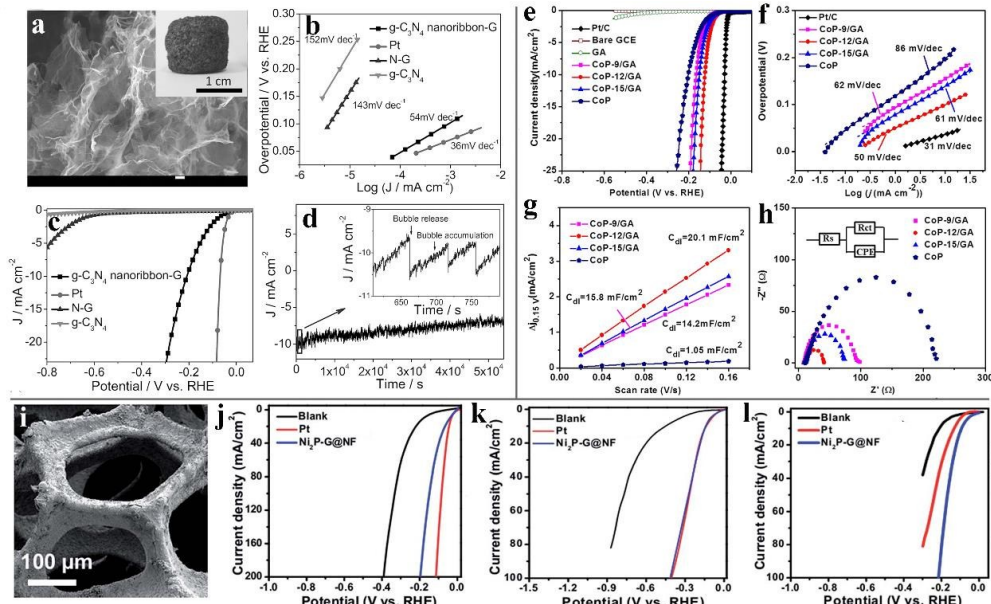


Figure 16. (a) SEM image and photograph of g-C₃N₄ nanoribbon-G, (b) Tafel plots, and (c) HER polarization curves using various catalysts. (d) The current density versus RHE of g-C₃N₄/GO,¹⁹⁶ (e) polarization curves for various samples, (f) Tafel plots for different samples, (g) capacitive current at 0.15 V, (h) Nyquist plots collected at a -200 mV bias voltage of GA/CoP,²⁰² (i) SEM image of nickel phosphide embedded within a graphene/nickel foam, polarization curves of nickel phosphide graphene/nickel foam in (j) 0.5 M H₂SO₄ (pH = 0), (k) 1 M KPi (pH = 7), and (l) 1 M KOH (pH = 14) of graphene/Ni foam.²⁰³

¹⁹⁴ Noble metal platinum is the most effective HER catalysts owing to the high current densities possible. Again, due to the relative scarcity and high cost of such noble metals, it is of great importance that new and inexpensive catalysts are developed for electrocatalytic HER. Owing to their high electrical conductivity, versatility, and stability, graphene aerogels are a promising for HER catalysis.¹⁹⁵ Qu et al. assembled graphene sheets containing graphitic carbon nitride (g-C₃N₄) nanoribbons into a 3D graphene aerogel (Figure 16a) resulting in superior HER activity with 54 mV decade⁻¹ for a Tafel slope, a lower onset overpotential of 80 mV and a current density of 10 mA cm⁻² at a 207 mV overpotential (Figure 16b).¹⁹⁶ The graphene analogue MoS has also emerged as a promising electrocatalyst due to its large BET and high electrical conductivity.^{197, 198} Zhou and Wang et al. concurrently researched GA/MoS₂ network composites and found that the material demonstrated excellent electrocatalysis of HER with a lower overpotential, higher catalytic current density, and improved stability.^{199, 200} Zhang et al. further functionalized GA/O-MWCNT with p-phenylenediamine-supported MoS₂ which has also shown excellent catalytic performance and stability.²⁰¹ Transition-metal phosphides (TMPs), such as CoP and Ni₂P, have attracted numerous attention as non-noble-metal catalysts for HER with high activity. Dong et al. prepared CoP/GA showing an overpotential of 121 mV at 10 mA cm⁻² and an exchange current density of 0.105 mA cm⁻² (Figure 16e-h).²⁰² Interested in expanding the understanding of the effects of pH on electrocatalysis, Du et al. designed a material composed of crystalline nickel phosphide embedded within a graphene/nickel foam. In extremely acid environments (pH = 0), there was a 30 mV overpotential (Figure 16j). Whereas in extremely basic environments (pH = 14), there was a 7 mV overpotential (Figure 16l).²⁰³



ARTICLE

The future of alternative fuel sources can take on several forms. In the case of HER, one is generating a high energy fuel (H_2) and using it to generate electricity through fuel cells and metal-air batteries. In contrast, one can also take an abundant waste product and convert it into useful products as is the case for CO_2 reduction. Electrolytic preparation of fuel from CO_2 reduction is a carbon-neutral energy cycle.²⁰⁴⁻²⁰⁶ Noble metals generally have good selectivity for CO_2 reduction. However, they have poor durability and are more scarce thus limiting their application.²⁰⁷ It remains a challenge to directly convert CO_2 into multi-carbon hydrocarbons (methane, ethylene) or oxygenates due to the absence of powerful, low cost catalysts.²⁰⁸ Graphene aerogels are a natural catalytic candidate for CO_2 reduction due to their 3D network structure, ease of fabrication, and high BET which enhances the interfacial contact with the electrolyte and adsorbed CO_2 . Further doping with nitrogen generates active sites with a low overpotential, good selectivity, and high durability toward CO_2 catalysis. Ajayan et al. manufactured N-GAs with an onset overpotential of -0.19 V for CO production, and at a lower overpotential (-0.47 V) than Au with a similar maximum Faradaic efficiency of CO formation (~85%) and higher stability (Figure 17).²⁰⁹

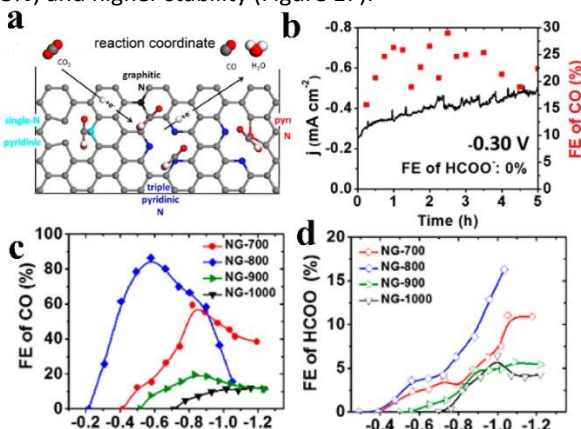


Figure 17. (a) CO_2 reduction pathway, (b) CO_2 reduction and CO production versus time and Faradaic efficiency, (c) CO versus potential, (d) $HCOO^-$ versus potential by DFT modelling of 3D graphene.²⁰⁹

4.3 Alcohol and Microbial Fuel Cells

Electro-oxidation of alcohol has also attracted interest due to the high energy conversion rate, low work temperature, easy storage and handling, low pollutant emission, and cost. Typically, Pt and Pd are the most commonly used catalysts in alcohol oxidation because of their excellent electrocatalytic performance.²¹⁰⁻²¹² Zhang et al. synthesized graphene oxide aerogel-supported Pt which facilitates reaction and avoids the

detrimental effect of reduced platinum active surface area. Furthermore, it was found that the electro-catalytic properties of GA/Pt were five times that of Pt/rGO (reduced graphene oxide) and 40% higher than that of commercial Pt/C (Figure 13).²¹³ Hui et al. prepared binder-free Pd/Graphene aerogel/Ni foam (Pd/GA/NF) electrodes that exhibited good electrocatalytic activity and an outstanding stability for alcohol electro-oxidation.²¹⁴ Fuel cells for direct alcohol conversion (such as ethanol, methanol, propanol, and butanol) have garnered much attention due to their operational safety, excellent energy density, low toxicity, and large-scale production potential.^{215, 216} However, the absence of appropriate anode materials, easy catalyst deactivation, and sluggish oxidation kinetics have greatly hindered their development. Liu et al. developed N-doped GA decorated with PtRu nanoparticles as a freestanding anode. The resulting power density and current density were 93 mW cm^{-2} and 426 mA cm^{-2} respectively (Figure 18).²¹⁷ This device indeed performs well, but the cost of intermetallic PtRu nanoparticles remains high. Hui et al. developed a similar 3D free-standing anode material composed of graphene aerogel decorated with nickel. Their devices recorded a lower current density of 6 mA cm^{-2} in 0.1 M ethanol and 0.1 M NaOH solution.²¹⁸ Clearly there remains an immense performance disparity between the noble metal and non-noble metal systems.

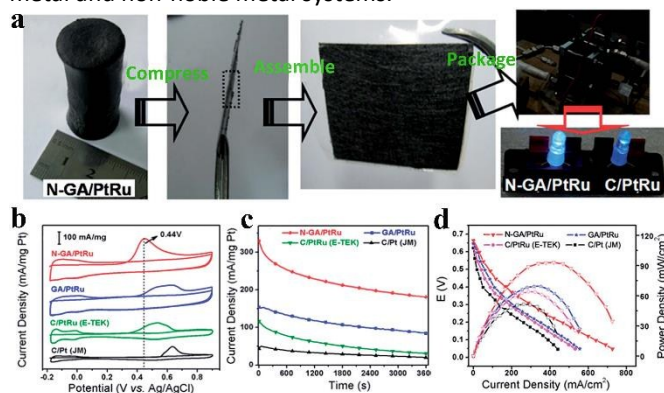


Figure 18. (a) Illustration of the fabrication of free standing electrodes and their incorporation into direct methanol fuel cells, (b) CV curves of various samples, (c) chronoamperometric curves of different samples, (d) electrochemical performance of direct methanol fuel cells constructed with various catalysts.²¹⁷

Microbial fuel cells (MFCs) are another type of fuel cell that relies on certain bacteria to convert organic waste into hydrogen for electricity generation.^{219, 220} From a theoretical standpoint, microbial fuel cells are ideal as they are using waste to generate electricity. However, poor energy conversion efficiency and low power densities limit their practical

application. The key component that is missing from microbial electrolysis cells (MECs) is a cost-effective catalyst for hydrogen production and bacterial adhesion.^{221, 222} Graphene is already being applied in conventional fuel cells due to its chemical inertness, excellent electrical conductivity and biocompatibility.²²³ The 3D network structure of graphene aerogels provides a large BET for bacterial adsorption and directed pathways for extracellular electron transfer and proton diffusion. Chen et al. prepared 3D MoS₂/N-GAs as a microbial electro-catalyst in which organic waste was oxidized by bacteria with generated electrons transferred to the cathode to reduce protons and generate hydrogen (Figure 19a-d), which achieved a high hydrogen production rate of 0.19 m³ H₂ m⁻³ d⁻¹.²²⁴ Chen et al. developed a polyaniline/graphene 3D network hybrid as a MFC anode. The cell had a power density of 190 mW m⁻² at 24 h with a maximum power density of 768 mW m⁻².²²⁵ Qiao et al.

synthesized a graphene aerogel by direct reduction of cysteine for a microbial fuel cell anode. The biocompatible, porous, and 3D structure of graphene aerogel afforded a maximum power density to 679.7 mW m⁻² and increased the loading of bacterial cells on the GA.²¹⁷ The large open pore structure and good biocompatibility are ideal for the effective immobilization, growth and cultivation of living microorganisms. The excellent conductivity promotes efficient current collection. When coupled with the high stability, these graphene aerogels may contribute to improved longevity toward the practical application of MFCs. Liu et al. reported 3D graphene aerogels homogeneously decorated with Pt nanoparticles for an MFC anode (Figure 19e-h). The MFC generated a maximum power density of 1460 mW m⁻²; enough to successfully power a kitchen timer (Figure 19h).²²⁶

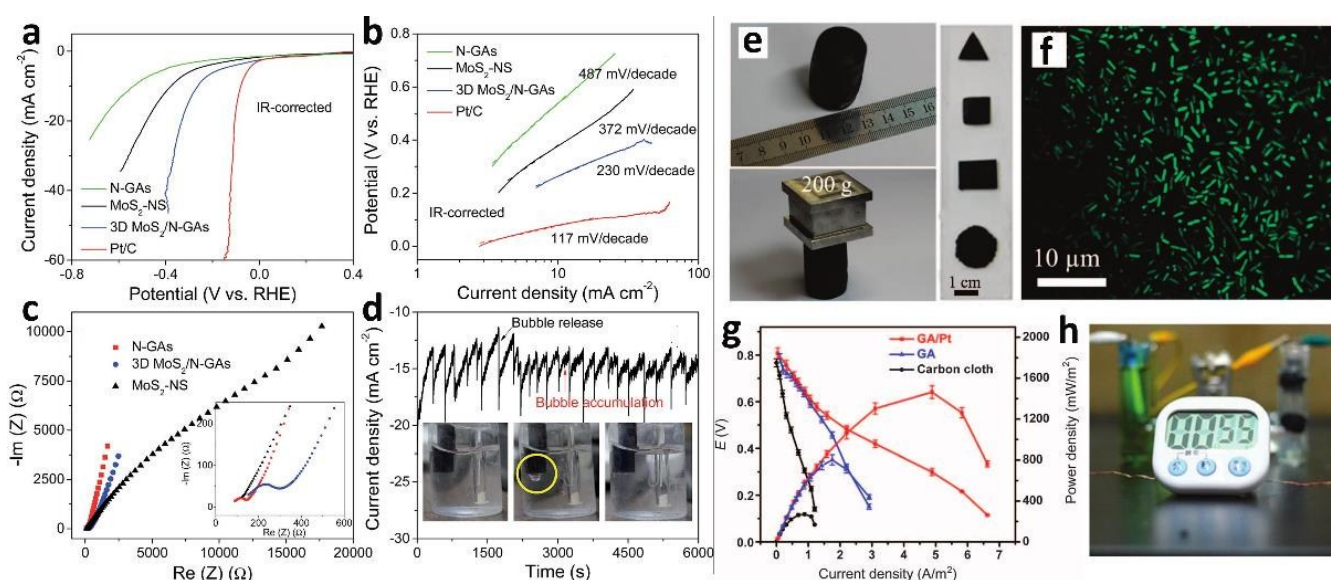


Figure 19. (a) Polarization curves, (b) Tafel plots, (c) EIS Nyquist plots of different samples, and (d) cathodic current density of 3D MoS₂/N-GA anodes for hydrogen evolution in microbial electrolysis cells.²²⁴ (e) Photograph of a graphene aerogel/Pt hybrids demonstrating high mechanical strength and shape control, (f) confocal microscope image of living bacteria inside the MFC after 3 days, (g) performance of MFCs with various electrode materials, and (h) photograph of an MFC driving a timer.^{225, 226}

4.4 Photocatalytic Water Splitting

In addition to bacterial-mediated generation of hydrogen, an obvious source of abundant hydrogen is water. Sunlight-driven photocatalytic and photoelectrochemical water splitting can produce hydrogen and oxygen in an environmentally friendly fashion.^{225, 227} Due to the large energy requirements to electrochemically split water, it is essential to develop novel and efficient photocatalysts with low-cost and high-stability.²²⁸ The key requirements for effective photoanodes include efficient light-trapping, excellent separation, fast OER kinetics, and fast transportation of photogenerated charge carriers.^{229, 230} For

these reasons, 3D network graphene materials are an ideal candidate for photoanode research. Chen et al. reported a graphene aerogel-based hybrid containing N-deficient g-C₃N₄/N-GA/Ni-Fe layered double hydroxide (DPCN/N-GA/Ni-Fe-LDH). This photoanode lead to effective separation and transport of photogenerated charge carriers with electrons/holes moving between the g-C₃N₄ and NiFe layers. The device showed photocurrent densities of 162.3 μA cm⁻² at 1.4 V with an incident photon-to-current efficiency (IPCE) of 2.5% at 350 nm during photo-electrocatalytic water splitting (Figure 20).²³¹

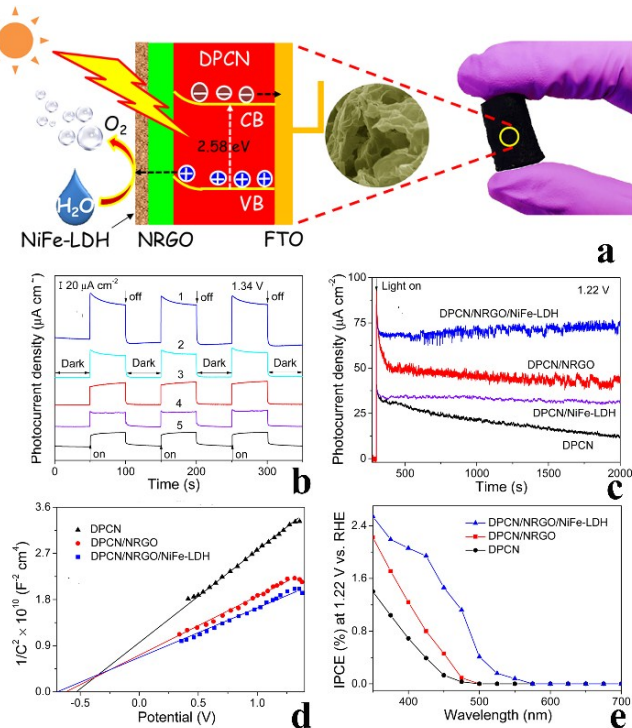
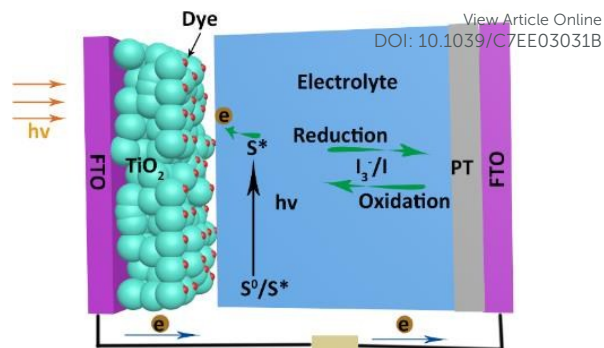


Figure 20. (a) Schematic illustration of the water oxidation pathway in graphene aerogel/g-C₃N₄/N-GA/NiFe cell, (b) transient photocurrent density versus time, (c) transient photocurrent responses of various samples, (d) Mott-Schottky plots, (e) IPCE spectra at 1.22 V under AM 1.5G irradiation of g-C₃N₄/N-Doped GA/NiFe.²³¹

4.5 Dye-sensitized and Perovskite Solar Cells

The direct conversion of solar energy into electricity is another promising area for renewable energy generation.^{232, 233} There are several different solar cell types being developed along these lines. An established type is the dye-sensitized solar cell (DSSC). DSSCs are composed of a working electrode, electrolyte, and counter electrode. DSSCs offer several advantages including large material availability and low cost.^{234, 235} The first solar cell was actually manufactured by Fritts in 1883 by making use of the photovoltaic effect. Bell Labs fabricated the first monocrystalline silicon solar cells in 1954 promoting the development of a variety of solar cells. Over the past 30 years, dye-sensitized solar cells have been developed with efficiencies up to 12% and excellent stability. The general operating mechanism of DSSCs is as follows: first, the adsorbed dye in the anode absorbs photons to generate electrons which are transported to the counter electrode leaving the dye in an oxidized state. Second, a redox couple reduces the oxidized dye with an electron thus refreshing the dye and leaving an oxidized redox couple. Lastly, the redox couple migrates to the counter electrode where it is reduced.²³⁶ The theory of dye-sensitized solar cells is shown in Scheme 5.



Scheme 5. Schematic diagram of DSSCs showing the sensitizer dye and iodide-triiodide redox couple.

The counter electrode (cathode) performs a crucial role in the DSSC system by catalyzing the reduction of the redox couple (typically an iodide-triiodide system) which serves as a mediator for refreshing the sensitizer dye. To improve the electrochemical performance of DSSCs, an ideal counter electrode must quickly transfer charges while also possessing high reducing strength. 3D graphene aerogel networks are a natural material for counter electrode development. Hu et al. developed a 3D honeycomb graphene structure by reaction between Li₂O and CO. The resulting 3D graphene aerogel counter electrode exhibited an energy conversion efficiency of 7.8%.²³⁷ Dai, Jang et al. fabricated N-doped graphene aerogel (Figure 21a, b) and P-doped graphene aerogel as metal-free counter electrodes for DSSCs with a power conversion efficiency up to 7.07% and 8.46%, respectively.^{238, 239} Conventional DSSCs use TiO₂ photoanodes in which trap states and random pathways often hinder electron transport and reduce efficiency. Moon et al. prepared a TiO₂-embedded graphene photoanode with a 3D porous structure that achieved a photon-to-electric conversion efficiency of 7.5%, a 55% increase over systems without graphene incorporation (Figure 21c).²⁴⁰ Conventional DSSCs typically use a liquid electrolyte with a power conversion efficiency around 12.3%.²⁴¹ The leakage of liquid electrolyte and evaporation of the organic solvent often limits the lifetime and can lead to reduced performance with time. For these reasons, solid electrolytes have also been investigated. Polymer gels are one class of solid electrolytes, but they suffer from relatively low charge transfer. To address this issue, researchers have begun doping solid electrolytes with conductive materials. Tang et al. modified poly(acrylic acid)-cetyltrimethylammonium bromide (PAA-CTAB) gel electrolytes with graphene to create a quasi-solid-state DSSCs (Figure 21, right panel). This technique combines the stability of the solid electrolytes with the rapid charge transfer of graphene to yield a high power conversion efficiency of 7.06% as compared to 6.07% for pure PAA-CTAB.²⁴²

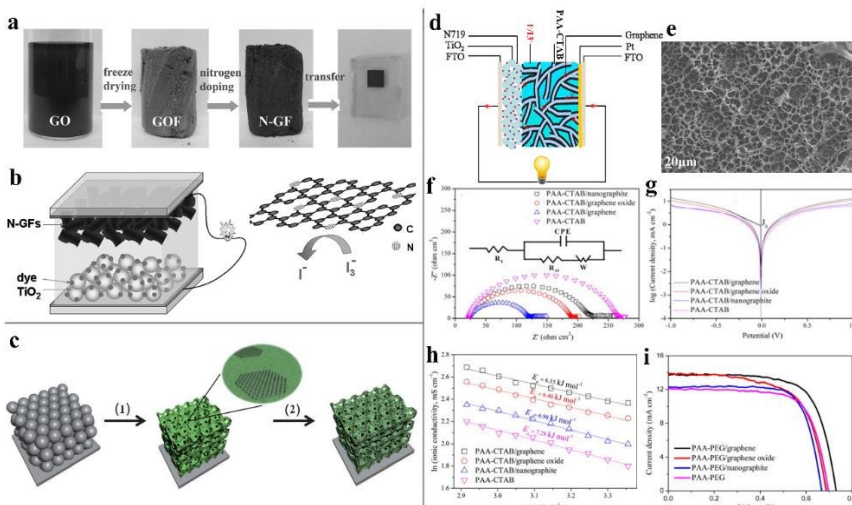


Figure 21. (a) Schematic illustration of the preparation process for graphene, (b) configuration of a DSSC and triiodide redox couple;²³⁹ (c) scheme for the fabrication of G-TiO₂ inverse opal electrodes: (1) colloidal PS spheres serve as templates, (2) graphene oxide is incorporated around spheres and reduced, (3) the PS spheres are dissolved away to yield a highly porous GO structure;²⁴⁰ (d) schematic illustration of a DSSC with a quasi-solid electrolyte composed of a PAA-CTAB gel and graphene, (e) SEM of porous structure, (f) Nyquist plots, (g) Tafel polarization curves, (h) Arrhenius plots, and (i) J-V characteristics of graphene gel on quasi-solid-state DSSCs.²⁴²

Perovskites are a recent rediscovery in the photovoltaics community that has attracted frenzied attention for solar cell applications due to their low cost, sizable absorption across the visible spectrum, narrow and widely tunable photoluminescence, and high photostability. As a result of these properties, theoretical conversion efficiencies as high as 28% may be possible.^{243–246} Organic–inorganic halide perovskite materials are suitable alternatives to conventional solar cell due to their high light absorption capability and long diffusion lengths. The development of graded bandgap materials is a promising approach to further increase solar spectrum utilization. Despite the considerable enhancement in electron–hole collection efficiency, satisfactory open-circuit output voltage and superior output current proved elusive. This is likely due to excessive cation mixing, which eliminates the graded bandgap. Many strategies have been implemented such as replacing the metal cations, varying the composition of halide ions, and altering the moisture content. Zettl et al. fabricated double perovskite layers (layer 1: CH₃NH₃SnI₃ and layer 2: CH₃NH₃PbI_{3-x}Br_x) incorporating GaN, hexagonal boron nitride (h-BN), and graphene aerogel.²⁴⁷ The cells reliably produce very high current densities up to 45 mA cm⁻² with average power conversion efficiencies of 18.41%. The graphene aerogel also serves as a barrier to moisture penetration as well as improve the perovskite film morphology (continuous films rather than perovskite islands).

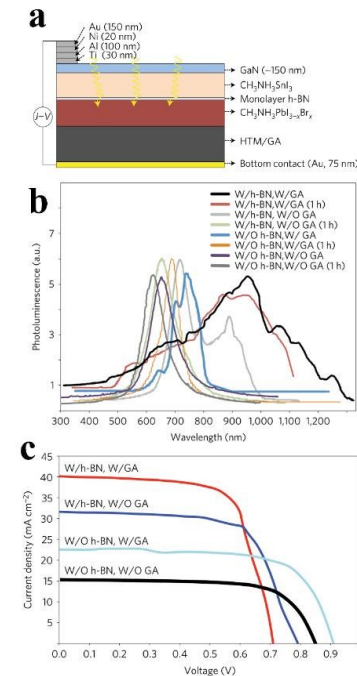


Figure 22. Schematic of a graded bandgap perovskite solar cell (i.e. two perovskite layers), (b) photoluminescence spectra of cells with (W/) and without (W/O) monolayer h-BN or GA components, (c) current density versus voltage of cells with and without h-BN or GA components.²⁴⁷

Conclusions and Outlook

A number of nanomaterials have been investigated for extensive applications in energy capture and energy storage. However, there are few nanomaterials that all exhibit the excellent performance, processability and abundance of graphene. Graphene has rapidly developed over the previous decade into a diverse assortment of types, composites and mixtures for countless applications. With the ever-present threat associated with depleted resources and environmental pollution, much attention has centred on developing various 3D nano-porous materials possessing large internal spaces, and high surface area. It is only natural then that combining 2D graphene with 3D porous networks as well as the direct formation of 3D graphene aerogels has attracted much attention. With endless material recipes currently being investigated, it is important to organize them into useful groups based on their different end uses.

In this review, we summarized the recent developments in the synthesis of 3D graphene networks and graphene aerogel compounds, and elaborated on their applications in energy capture, storage, and conversion. Graphene aerogels are especially attractive due to the large number of synthesis techniques including self-assembly (reducing, hydrothermal, metal ions), cross-linkers (organic and inorganic), CVD-growth (with or without template), and 3D printing. In double-layer capacitors, graphene aerogels can be directly substituted for or incorporated with other carbon materials (CNTs, porous carbon, carbon bulk) as electrode materials to enable high power densities and large cycle lifetimes. The electrochemical performance of graphene aerogel electrodes could also be enhanced by increasing the specific surface area, increasing the

electrical conductivity, increasing the porosity, and doping/co-doping with various non-metals including N,¹⁰ P,¹¹ S,¹² and B.¹³ In pseudocapacitors, graphene aerogel was employed as an anode. Subsequent modification with metal compounds (single/binary metal oxides, metal hydroxides), and conducting polymers (polypyrrole, polyaniline) lead to enhanced energy density compared to double layer capacitors. Unlike ion migration in pseudo-capacitors in which reactions largely occur on the surface of the electrodes, in graphene aerogel electrodes ions can insert and diffuse into the solid phase of the electrode leading to higher energy densities. For fuel cells, GAs can serve as catalyst for electrolysis cells promoting the generation of fuel from water (HER), organic waste (MFCs), and alcohol. GAs can also function as a cathode for fuel cell systems (hydrogen, alcohol, microbial fuel cells) by catalyzing reduction reactions. For solar cells, GAs can be used as a counter electrode, a component in electrolyte gels for quasi-solid-state DSSCs, as a moisture barrier, and scaffold material for HTMs in perovskite solar cells to improve performance and stability.

It is clear that graphene aerogels and graphene aerogel-modified materials show much promise and application in energy capture, storage, and conversion technologies. Despite this, there remain some developmental hurdles to be overcome in transitioning from the lab to real world applications. First, synthetic methods and post-treatments need to be optimized to improve the surface area of graphene aerogels and increase the porosity. Fortunately, the material cost of graphene-based materials is substantially lower than that of traditional noble metal catalysts. It is the development and/or repurposing of new and existing industrial scale technology that will limit the time it takes to see graphene-based materials make the jump into energy capture, conversion and storage technologies.

Table 1. Performance Characteristics of Graphene Aerogel Composite Materials for Supercapacitors

Materials	Specific capacitance (F g^{-1})	Cycle retention	Voltage window (V)	Current load or scan rate (A g^{-1})	Ref
Macro-/mesoporous GA	226	100% after 5000 cycles	0-0.8	N.A.	66
N-doped GA	113.8	91% after 4000 cycles	0-1.0	185	54
GA/carbon bulk	231	99% after 5000 cycles	0-3.5	1.0	248
GA anode & MnO_2 -Ni cathode	157.7	83% after 5000 cycles	0-2.0	1.0	71
GA anode & NiO cathode	210	95% after 3000 cycles	-1.2-0.5	3.1	72
GA/ Co_3O_4	768	143% after 500 cycles	0-0.5	10	77
GA/NiO	745	100% after 2000 cycles	0-0.5	1.4	34
GA/ MnO_2	175	81% after 5000 cycles	0-1.0	N.A.	249
GA/ Ni(OH)_2	119	63.2% after 10000 cycles	0-0.5	1.0	250
GA/ CoMoO_4	2741	96.36% after 10000 cycles	0-0.9	1.43	80
GA/ TiO_2	206.7	96.4% after 150 cycles	-0.2-0.8	0.5	251
GA/ZnO	316	99% after 1000 cycles	0-0.5	6.7	252
N-GA/CNTs	180	96% after 3000 cycles	-1.0-0	0.5	253
GA/MWNT	286	99.34% after 85000 cycles	N.A.	N.A.	254

GA/Ag Nanowire/Carbon	213	>90% after 10000 cycles	0-1.0	N.A.	255	View Article Online DOI: 10.1039/C7EE03031B
GA/polyaniline	463	90.6% after 500 cycles	0-0.4	1.0	85	
GA/Co(OH) ₂	1139	N.A.	0-1.2	10	77	
GA/Polyaniline/Co ₃ O ₄	1247	80% after 6000 cycles	0-0.4	1.0	87	
GA/polypyrrole	350	N.A.	0-1.0	1.5	84	

Table 2. Performance Characteristics of Graphene Aerogel Composite Materials for Lithium-based Batteries

Materials	Type	Capacity	Cycling	Ref
LiFePO ₄ /GA	Cathode of Li-ion battery	78 mA h g ⁻¹ @100 C	89% after 1000 cycles@10 C	95
O ₂ /GA	Cathode of Li-O ₂ battery	11060 mA h g ⁻¹ @280 mA g ⁻¹	N.A.	100
S/GA	Cathode of Li-S battery	10.3 mA h cm ⁻² @0.2 C	63.8% after 350 cycles	105
Te/GA	Cathode of Li-Te battery	2611 mA h cm ⁻² @0.2 C	88% after 250 cycles	108
Fe ₃ O ₄ /GA	Anode of Li-ion battery	1060 mA h g ⁻¹ @93 mA g ⁻¹	1059 mA h g ⁻¹ after 150 cycle	126
TiO ₂ /GA	Anode of Li-ion battery	605 mA h g ⁻¹ @100 mA g ⁻¹	80% after 50 cycles	123
Fe ₂ O ₃ /GA	Anode of Li-ion battery	995 mA h g ⁻¹ @100 mA g ⁻¹	995 mA h g ⁻¹ after 50 cycles	122
Co ₃ O ₄ /GA	Anode of Li-ion battery	1012 mA h g ⁻¹ @100 mA g ⁻¹	1012 mA h g ⁻¹ after 100 cycles	125
CuO/GA/CNTs	Anode of Li-ion battery	753 mA h g ⁻¹ @0.1 C	639 mA h g ⁻¹ after 80 cycles	256
Bi ₂ O ₃ /GA	Anode of Li-ion battery	273 mA h g ⁻¹ @10000 mA g ⁻¹	417 mA h g ⁻¹ after 100 cycle @200 C	124
C/MoS ₂ /N-GA	Anode of Li-ion battery	1600 mA h g ⁻¹ @200 mA g ⁻¹	900 mA h g ⁻¹ after 500 cycle	257
ZnO/GA	Anode of Li-ion battery	415 mA h g ⁻¹ @1000 mA g ⁻¹	490 mA h g ⁻¹ after 100 cycle@100 C	258
MoS ₂ /GA	Anode of Li-ion battery	1235 mA h g ⁻¹ @200 mA g ⁻¹	85.8% after 60 cycle@80 C	259
Si/GA	Anode of Li-ion battery	963 mA h g ⁻¹ @1.5 mg cm ⁻²	370 mA h g ⁻¹ after 100 cycle	260
SiO ₂	Anode of Li-ion battery	300 mA h g ⁻¹ @500 mA g ⁻¹		137
Sn/GA	Anode of Li-ion battery	1022 mA h g ⁻¹ @200 mA g ⁻¹	96.3% after 1000 cycles	138
SnO ₂ /GA	Anode of Li-ion battery	1299 mA h g ⁻¹ @100 mA g ⁻¹	148% after 450 cycle	261

Acknowledgements

The authors thank the National Natural Science Foundation of China (21501127 and 51502185), the Natural Science Foundation of Jiangsu Province of China (BK20140400). We also acknowledge the funds from the Priority Academic Program Development of Jiangsu Higher Education Institutions (PAPD), and Project for Jiangsu Scientific and Technological Innovation Team (2013).

References:

- W. Geng, Z. Ming, P. Lilin, L. Ximei, L. Bo and D. Jinhui, *Renew. Sust. Energy. Rev.*, 2016, **53**, 885-896.
- M. Brauer, G. Freedman, J. Frostad, A. van Donkelaar, R. V. Martin, F. Dentener, R. van Dingenen, K. Estep, H. Amini, J. S. Apte, K. Balakrishnan, L. Barregard, D. Broday, V. Feigin, S. Ghosh, P. K. Hopke, L. D. Knibbs, Y. Kokubo, Y. Liu, S. Ma, L. Morawska, J. L. Sangrador, G. Shaddick, H. R. Anderson, T. Vos, M. H. Forouzanfar, R. T. Burnett and A. Cohen, *Environ. Sci. Technol.*, 2016, **50**, 79-88.
- S. Rao, Z. Klimont, S. J. Smith, R. Van Dingenen, F. Dentener, L. Bouwman, K. Riahi, M. Amann, B. L. Bodirsky and D. P. van Vuuren, *Global Environ. Change*, 2017, **42**, 346-358.
- V. R. Stamenkovic, D. Strmcnik, P. P. Lopes and N. M. Markovic, *Nat. Mater.*, 2016, **16**, 57-69.
- J. L. Bredas, E. H. Sargent and G. D. Scholes, *Nat. Mater.*, 2016, **16**, 35-44.
- S. Chu, Y. Cui and N. Liu, *Nat. Mater.*, 2016, **16**, 16-22.
- M. A. Green and S. P. Bremner, *Nat. Mater.*, 2016, **16**, 23-34.
- C. P. Grey and J. M. Tarascon, *Nat. Mater.*, 2016, **16**, 45-56.
- J. H. Montoya, L. C. Seitz, P. Chakthranont, A. Vojvodic, T. F. Jaramillo and J. K. Norskov, *Nat. Mater.*, 2016, **16**, 70-81.
- P. Simon and Y. Gogotsi, *Nat. Mater.*, 2008, **7**, 845-854.
- M. Winter and R. J. Brodd, *Chem. Rev.*, 2004, **104**,

ARTICLE

Journal Name

- 4245-4269.
12. G. P. Wang, L. Zhang and J. J. Zhang, *Chem. Soc. Rev.*, 2012, **41**, 797-828.
13. J. M. Tarascon and M. Armand, *Nature*, 2001, **414**, 359-367.
14. P. G. Bruce, B. Scrosati and J. M. Tarascon, *Angew. Chem., Int. Ed.*, 2008, **47**, 2930-2946.
15. K. S. Novoselov, A. K. Geim, S. V. Morozov, D. Jiang, Y. Zhang, S. V. Dubonos, I. V. Grigorieva and A. A. Firsov, *Science*, 2004, **306**, 666-669.
16. S. Stankovich, D. A. Dikin, R. D. Piner, K. A. Kohlhaas, A. Kleinhammes, Y. Jia, Y. Wu, S. T. Nguyen and R. S. Ruoff, *Carbon*, 2007, **45**, 1558-1565.
17. X. S. Li, W. W. Cai, J. H. An, S. Kim, J. Nah, D. X. Yang, R. Piner, A. Velamakanni, I. Jung, E. Tutuc, S. K. Banerjee, L. Colombo and R. S. Ruoff, *Science*, 2009, **324**, 1312-1314.
18. F. Bonaccorso, Z. Sun, T. Hasan and A. C. Ferrari, *Nat. Photonics*, 2010, **4**, 611-622.
19. D. S. Hecht, L. B. Hu and G. Irvin, *Adv. Mater.*, 2011, **23**, 1482-1513.
20. Y. Zhang, L. Y. Zhang and C. W. Zhou, *Acc. Chem. Res.*, 2013, **46**, 2329-2339.
21. J. Kim, L. J. Cote and J. X. Huang, *Acc. Chem. Res.*, 2012, **45**, 1356-1364.
22. S. Nardeccchia, D. Carriazo, M. L. Ferrer, M. C. Gutierrez and F. del Monte, *Chem. Soc. Rev.*, 2013, **42**, 794-830.
23. Y. F. Ma and Y. S. Chen, *Natl. Sci. Rev.*, 2015, **2**, 40-53.
24. Y. X. Xu, K. X. Sheng, C. Li and G. Q. Shi, *ACS Nano*, 2010, **4**, 4324-4330.
25. W. Chen and L. Yan, *Nanoscale*, 2011, **3**, 3132-3137.
26. H. P. Cong, X. C. Ren, P. Wang and S. H. Yu, *ACS Nano*, 2012, **6**, 2693-2703.
27. Z. S. Wu, S. Yang, Y. Sun, K. Parvez, X. Feng and K. Mullen, *J. Am. Chem. Soc.*, 2012, **134**, 9082-9085.
28. J. Mao, M. Ge, J. Huang, Y. Lai, C. Lin, K. Zhang, K. Meng and Y. Tang, *J. Mater. Chem. A*, 2017, **5**, 11873-11881.
29. H. Y. Sun, Z. Xu and C. Gao, *Adv. Mater.*, 2013, **25**, 2554-2560.
30. H. L. Gao, Y. B. Zhu, L. B. Mao, F. C. Wang, X. S. Luo, Y. Y. Liu, Y. Lu, Z. Pan, J. Ge, W. Shen, Y. R. Zheng, L. Xu, L. J. Wang, W. H. Xu, H. A. Wu and S. H. Yu, *Nat. Commun.*, 2016, **7**, 12920.
31. J. Bai, A. Zhou, Z. Huang, J. Wu, H. Bai and L. Li, *J. Mater. Chem. A*, 2015, **3**, 22687-22694.
32. K. Z. Gao, Z. Q. Shao, J. Li, X. Wang, X. Q. Peng, W. J. Wang and F. J. Wang, *J. Mater. Chem. A*, 2013, **1**, 63-67.
33. M. A. Worsley, P. J. Pauzauskie, T. Y. Olson, J. Biener, J. H. Satcher and T. F. Baumann, *J. Am. Chem. Soc.*, 2010, **132**, 14067-14069.
34. X. Cao, Y. Shi, W. Shi, G. Lu, X. Huang, Q. Yan, Q. Zhang and H. Zhang, *Small*, 2011, **7**, 3163-3168.
35. X. Wang, Y. Zhang, C. Zhi, X. Wang, D. Tang, Y. Xu, Q. 4245-4269.
36. C. Zhu, T. Y. J. Han, E. B. Duoss, A. M. Golobic, J. D. Kuntz, C. M. Spadaccini and M. A. Worsley, *Nat. Commun.*, 2015, **6**, 8.
37. M. D. Stoller, S. J. Park, Y. W. Zhu, J. H. An and R. S. Ruoff, *Nano Lett.*, 2008, **8**, 3498-3502.
38. B. E. Conway, *J. Electrochem. Soc.*, 1991, **138**, 1539-1548.
39. S. Chen, J. W. Zhu, X. D. Wu, Q. F. Han and X. Wang, *ACS Nano*, 2010, **4**, 2822-2830.
40. M. F. El-Kady, V. Strong, S. Dubin and R. B. Kaner, *Science*, 2012, **335**, 1326-1330.
41. D. A. Dikin, S. Stankovich, E. J. Zimney, R. D. Piner, G. H. B. Dommett, G. Evmenenko, S. T. Nguyen and R. S. Ruoff, *Nature*, 2007, **448**, 457-460.
42. Q. Wu, Y. X. Xu, Z. Y. Yao, A. R. Liu and G. Q. Shi, *ACS Nano*, 2010, **4**, 1963-1970.
43. H. L. Wang, H. S. Casalongue, Y. Y. Liang and H. J. Dai, *J. Am. Chem. Soc.*, 2010, **132**, 7472-7477.
44. X. Zhang, Y. K. Lai, M. Z. Ge, Y. X. Zheng, K. Q. Zhang and Z. Q. Lin, *J. Mater. Chem. A*, 2015, **3**, 12761-12768.
45. L. Zhang and G. Q. Shi, *J. Phys. Chem. C*, 2011, **115**, 17206-17212.
46. V. H. Luan, H. N. Tien, L. T. Hoa, T. M. H. Nguyen, E. S. Oh, J. Chung, E. J. Kim, W. M. Choi, B. S. Kong and S. H. Hur, *J. Mater. Chem. A*, 2013, **1**, 208-211.
47. L. Zhang, X. Li, M. Wang, Y. He, L. Chai, J. Huang, H. Wang, X. Wu and Y. Lai, *ACS Appl. Mater. Interfaces*, 2016, **8**, 34638-34647.
48. C. D. Wang, D. B. Liu, S. M. Chen, Y. Sang, Y. A. Haleem, C. Q. Wu, W. Y. Xu, Q. Fang, M. Habib, J. Cao, Z. Q. Niu, P. M. Ajayan and L. Song, *Small*, 2016, **12**, 5684-5691.
49. Y. Q. Qian, I. M. Ismail and A. Stein, *Carbon*, 2014, **68**, 221-231.
50. D. Hulicova-Jurcakova, A. M. Puziy, O. I. Poddubnaya, F. Suarez-Garcia, J. M. D. Tascon and G. Q. Lu, *J. Am. Chem. Soc.*, 2009, **131**, 5026-5027.
51. H. M. Jeong, J. W. Lee, W. H. Shin, Y. J. Choi, H. J. Shin, J. K. Kang and J. W. Choi, *Nano Lett.*, 2011, **11**, 2472-2477.
52. Z. S. Wu, A. Winter, L. Chen, Y. Sun, A. Turchanin, X. L. Feng and K. Mullen, *Adv. Mater.*, 2012, **24**, 5130-5135.
53. Z. H. Wen, X. C. Wang, S. Mao, Z. Bo, H. Kim, S. M. Cui, G. H. Lu, X. L. Feng and J. H. Chen, *Adv. Mater.*, 2012, **24**, 5610-5616.
54. P. Chen, J.-J. Yang, S.-S. Li, Z. Wang, T.-Y. Xiao, Y.-H. Qian and S.-H. Yu, *Nano Energy*, 2013, **2**, 249-256.
55. P. Hao, Z. Zhao, Y. Leng, J. Tian, Y. Sang, R. I. Boughton, C. P. Wong, H. Liu and B. Yang, *Nano Energy*, 2015, **15**, 9-23.
56. D. Sheberla, J. C. Bachman, J. S. Elias, C.-J. Sun, Y. Shao-Horn and M. Dinca, *Nat. Mater.*, 2017, **16**, 220-224.
57. J. H. Hou, C. B. Cao, F. Idrees and X. L. Ma, *ACS Nano*, 2015, **9**, 2556-2564.

Journal Name

ARTICLE

58. Y. W. Zhu, S. Murali, M. D. Stoller, K. J. Ganesh, W. W. Cai, P. J. Ferreira, A. Pirkle, R. M. Wallace, K. A. Cychosz, M. Thommes, D. Su, E. A. Stach and R. S. Ruoff, *Science*, 2011, **332**, 1537-1541.
59. X. Sun, P. Cheng, H. Wang, H. Xu, L. Dang, Z. Liu and Z. Lei, *Carbon*, 2015, **92**, 1-10.
60. K. S. Kim, Y. Zhao, H. Jang, S. Y. Lee, J. M. Kim, K. S. Kim, J. H. Ahn, P. Kim, J. Y. Choi and B. H. Hong, *Nature*, 2009, **457**, 706-710.
61. S. Ye, J. Feng and P. Wu, *ACS Appl. Mater. Interfaces*, 2013, **5**, 7122-7129.
62. A. G. Pandolfo and A. F. Hollenkamp, *J. Power Sources*, 2006, **157**, 11-27.
63. J. S. Lee, S. I. Kim, J. C. Yoon and J. H. Jang, *ACS Nano*, 2013, **7**, 6047-6055.
64. Y. J. Lee, G.-P. Kim, Y. Bang, J. Yi, J. G. Seo and I. K. Song, *Mater. Res. Bull.*, 2014, **50**, 240-245.
65. S. Yun, S. O. Kang, S. Park and H. S. Park, *Nanoscale*, 2014, **6**, 5296-5302.
66. Z. S. Wu, Y. Sun, Y. Z. Tan, S. Yang, X. Feng and K. Mullen, *J. Am. Chem. Soc.*, 2012, **134**, 19532-19535.
67. C. Zhu, T. Liu, F. Qian, T. Y. Han, E. B. Duoss, J. D. Kuntz, C. M. Spadaccini, M. A. Worsley and Y. Li, *Nano Lett.*, 2016, **16**, 3448-3456.
68. X. H. Xia, J. P. Tu, Y. Q. Zhang, X. L. Wang, C. D. Gu, X. B. Zhao and H. J. Fan, *ACS Nano*, 2012, **6**, 5531-5538.
69. H. B. Li, M. H. Yu, F. X. Wang, P. Liu, Y. Liang, J. Xiao, C. X. Wang, Y. X. Tong and G. W. Yang, *Nat. Commun.*, 2013, **4**, 7.
70. D. A. C. Brownson, D. K. Kampouris and C. E. Banks, *J. Power. Sources*, 2011, **196**, 4873-4885.
71. H. Gao, F. Xiao, C. B. Ching and H. Duan, *ACS Appl. Mater. Interfaces*, 2012, **4**, 2801-2810.
72. F. Luan, G. Wang, Y. Ling, X. Lu, H. Wang, Y. Tong, X. X. Liu and Y. Li, *Nanoscale*, 2013, **5**, 7984-7990.
73. G. H. Yu, L. B. Hu, N. A. Liu, H. L. Wang, M. Vosgueritchian, Y. Yang, Y. Cui and Z. A. Bao, *Nano Lett.*, 2011, **11**, 4438-4442.
74. Y. Xu, X. Huang, Z. Lin, X. Zhong, Y. Huang and X. Duan, *Nano Research*, 2012, **6**, 65-76.
75. C. Zhou, Y. W. Zhang, Y. Y. Li and J. P. Liu, *Nano Lett.*, 2013, **13**, 2078-2085.
76. K. Lu, J. T. Zhang, Y. Q. Wang, J. Z. Ma, B. Song and H. Y. Ma, *ACS Sustain. Chem. Eng.*, 2017, **5**, 821-827.
77. X. C. Dong, H. Xu, X. W. Wang, Y. X. Huang, M. B. Chan-Park, H. Zhang, L. H. Wang, W. Huang and P. Chen, *ACS Nano*, 2012, **6**, 3206-3213.
78. U. M. Patil, S. C. Lee, J. S. Sohn, S. B. Kulkarni, K. V. Gurav, J. H. Kim, J. H. Kim, S. Lee and S. C. Jun, *Electrochim. Acta*, 2014, **129**, 334-342.
79. L. Q. Mai, F. Yang, Y. L. Zhao, X. Xu, L. Xu and Y. Z. Luo, *Nat. Commun.*, 2011, **2**, 5.
80. X. Yu, B. Lu and Z. Xu, *Adv. Mater.*, 2014, **26**, 1044-1051.
81. G. A. Snook, P. Kao and A. S. Best, *J. Power. Sources*, 2011, **196**, 1-12.
82. L. Z. Fan and J. Maier, *Electrochim. Commun.*, 2006, **8**, 937-940.
View Article Online
DOI: 10.1039/C7EE03031B
83. H. Moon, H. Lee, J. Kwon, Y. D. Suh, D. K. Kim, I. Ha, J. Yeo, S. Hong and S. H. Ko, *Sci. Rep.*, 2017, **7**, 41981.
84. Y. Zhao, J. Liu, Y. Hu, H. Cheng, C. Hu, C. Jiang, L. Jiang, A. Cao and L. Qu, *Adv. Mater.*, 2013, **25**, 591-595.
85. K. Chi, Z. Zhang, J. Xi, Y. Huang, F. Xiao, S. Wang and Y. Liu, *ACS Appl. Mater. Interfaces*, 2014, **6**, 16312-16319.
86. L. Wang, H. Yang, X. Liu, R. Zeng, M. Li, Y. Huang and X. Hu, *Angew. Chem., Int. Ed.*, 2017, **56**, 1105-1110.
87. H. Lin, Q. Huang, J. Wang, J. Jiang, F. Liu, Y. Chen, C. Wang, D. Lu and S. Han, *Electrochim. Acta*, 2016, **191**, 444-451.
88. P. F. Yan, J. M. Zheng, M. Gu, J. Xiao, J. G. Zhang and C. M. Wang, *Nat. Commun.*, 2017, **8**, 9.
89. M. Gu, I. Belharouak, J. M. Zheng, H. M. Wu, J. Xiao, A. Genc, K. Amine, S. Thevuthasan, D. R. Baer, J. G. Zhang, N. D. Browning, J. Liu and C. M. Wang, *ACS Nano*, 2013, **7**, 760-767.
90. S. Kuppan, Y. Xu, Y. Liu and G. Chen, *Nat. Commun.*, 2017, **8**, 14309.
91. A. K. Padhi, K. S. Nanjundaswamy and J. B. Goodenough, *J. Electrochem. Soc.*, 1997, **144**, 1188-1194.
92. B. Kang and G. Ceder, *Nature*, 2009, **458**, 190-193.
93. L. X. Yuan, Z. H. Wang, W. X. Zhang, X. L. Hu, J. T. Chen, Y. H. Huang and J. B. Goodenough, *Energy Environ. Sci.*, 2011, **4**, 269-284.
94. H. Liu, F. C. Strobridge, O. J. Borkiewicz, K. M. Wiaderek, K. W. Chapman, P. J. Chupas and C. P. Grey, *Science*, 2014, **344**, 7.
95. B. Wang, W. Al Abdulla, D. Wang and X. S. Zhao, *Energy Environ. Sci.*, 2015, **8**, 869-875.
96. Z. Q. Peng, S. A. Freunberger, Y. H. Chen and P. G. Bruce, *Science*, 2012, **337**, 563-566.
97. J. Lu, Y. J. Lee, X. Y. Luo, K. C. Lau, M. Asadi, H. H. Wang, S. Brombosz, J. G. Wen, D. Y. Zhai, Z. H. Chen, D. J. Miller, Y. S. Jeong, J. B. Park, Z. Z. Fang, B. Kumar, A. Salehi-Khojin, Y. K. Sun, L. A. Curtiss and K. Amine, *Nature*, 2016, **529**, 377-382.
98. J. Xiao, D. H. Mei, X. L. Li, W. Xu, D. Y. Wang, G. L. Graff, W. D. Bennett, Z. M. Nie, L. V. Saraf, I. A. Aksay, J. Liu and J. G. Zhang, *Nano Lett.*, 2011, **11**, 5071-5078.
99. S. R. Younesi, S. Urbonaite, F. Bjorefors and K. Edstrom, *J. Power. Sources*, 2011, **196**, 9835-9838.
100. Z.-L. Wang, D. Xu, J.-J. Xu, L.-L. Zhang and X.-B. Zhang, *Adv. Funct. Mater.*, 2012, **22**, 3699-3705.
101. X. L. Ji, K. T. Lee and L. F. Nazar, *Nat. Mater.*, 2009, **8**, 500-506.
102. Z. Yuan, H. J. Peng, T. Z. Hou, J. Q. Huang, C. M. Chen, D. W. Wang, X. B. Cheng, F. Wei and Q. Zhang, *Nano Lett.*, 2016, **16**, 519-527.
103. J. Nelson, S. Misra, Y. Yang, A. Jackson, Y. J. Liu, H. L. Wang, H. J. Dai, J. C. Andrews, Y. Cui and M. F. Toney, *J. Am. Chem. Soc.*, 2012, **134**, 6337-6343.

ARTICLE

Journal Name

104. Z. W. Seh, W. Y. Li, J. J. Cha, G. Y. Zheng, Y. Yang, M. T. McDowell, P. C. Hsu and Y. Cui, *Nat. Commun.*, 2013, **4**, 6.
105. G. Hu, C. Xu, Z. Sun, S. Wang, H. M. Cheng, F. Li and W. Ren, *Adv. Mater.*, 2016, **28**, 1603-1609.
106. C. P. Yang, S. Xin, Y. X. Yin, H. Ye, J. Zhang and Y. G. Guo, *Angew. Chem., Int. Ed.*, 2013, **52**, 8363-8367.
107. N. Ding, S. F. Chen, D. S. Geng, S. W. Chien, T. An, T. S. A. Hor, Z. L. Liu, S. H. Yu and Y. Zong, *Adv. Energy Mater.*, 2015, **5**, 7.
108. J. He, Y. Chen, W. Lv, K. Wen, Z. Wang, W. Zhang, Y. Li, W. Qin and W. He, *ACS Nano*, 2016, **10**, 8837-8842.
109. G. M. Zhou, E. Paek, G. S. Hwang and A. Manthiram, *Nat. Commun.*, 2015, **6**, 11.
110. J. B. Goodenough and Y. Kim, *Chem. Mat.*, 2010, **22**, 587-603.
111. E. Yoo, J. Kim, E. Hosono, H. Zhou, T. Kudo and I. Honma, *Nano Lett.*, 2008, **8**, 2277-2282.
112. Z. S. Wu, W. C. Ren, L. Wen, L. B. Gao, J. P. Zhao, Z. P. Chen, G. M. Zhou, F. Li and H. M. Cheng, *ACS Nano*, 2010, **4**, 3187-3194.
113. H. L. Wang, L. F. Cui, Y. A. Yang, H. S. Casalongue, J. T. Robinson, Y. Y. Liang, Y. Cui and H. J. Dai, *J. Am. Chem. Soc.*, 2010, **132**, 13978-13980.
114. G. M. Zhou, D. W. Wang, F. Li, L. L. Zhang, N. Li, Z. S. Wu, L. Wen, G. Q. Lu and H. M. Cheng, *Chem. Mat.*, 2010, **22**, 5306-5313.
115. C. K. Chan, H. L. Peng, G. Liu, K. McIlwrath, X. F. Zhang, R. A. Huggins and Y. Cui, *Nat. Nanotechnol.*, 2008, **3**, 31-35.
116. Y. C. Liu, N. Zhang, L. F. Jiao, Z. L. Tao and J. Chen, *Adv. Funct. Mater.*, 2015, **25**, 214-220.
117. J. Jiang, Y. Y. Li, J. P. Liu, X. T. Huang, C. Z. Yuan and X. W. Lou, *Adv. Mater.*, 2012, **24**, 5166-5180.
118. V. Etacheri, R. Marom, R. Elazari, G. Salitra and D. Aurbach, *Energy Environ. Sci.*, 2011, **4**, 3243-3262.
119. G. X. Wang, X. P. Shen, J. Yao and J. Park, *Carbon*, 2009, **47**, 2049-2053.
120. Z. S. Wu, W. C. Ren, L. Xu, F. Li and H. M. Cheng, *ACS Nano*, 2011, **5**, 5463-5471.
121. X. J. Zhu, Y. W. Zhu, S. Murali, M. D. Stollers and R. S. Ruoff, *ACS Nano*, 2011, **5**, 3333-3338.
122. L. Xiao, D. Wu, S. Han, Y. Huang, S. Li, M. He, F. Zhang and X. Feng, *ACS Appl. Mater. Interfaces*, 2013, **5**, 3764-3769.
123. B. Qiu, M. Xing and J. Zhang, *J. Am. Chem. Soc.*, 2014, **136**, 5852-5855.
124. W. Fang, N. Zhang, L. Fan and K. Sun, *J. Power. Sources*, 2016, **333**, 30-36.
125. M. A. Garakani, S. Abouali, B. Zhang, C. A. Takagi, Z. L. Xu, J. Q. Huang, J. Huang and J. K. Kim, *ACS Appl. Mater. Interfaces*, 2014, **6**, 18971-18980.
126. W. Wei, S. Yang, H. Zhou, I. Lieberwirth, X. Feng and K. Mullen, *Adv. Mater.*, 2013, **25**, 2909-2914.
127. H. Sun, L. Mei, J. Liang, Z. Zhao, C. Lee, H. Fei, M. Ding, J. Lau, M. Li and C. Wang, *Science*, 2017, **356**, 599-604.
128. J. L. Lang, B. Ding, T. Zhu, H. X. Su, H. Luo, L. H. Qi, K. Liu, K. Wang, N. Hussain, C. S. Zhao, X. Li, H. J. Gao and H. Wu, *Adv. Mater.*, 2016, **28**, 10236-10243.
129. U. Kasavajjula, C. S. Wang and A. J. Appleby, *J. Power. Sources*, 2007, **163**, 1003-1039.
130. X. W. Lou, Y. Wang, C. L. Yuan, J. Y. Lee and L. A. Archer, *Adv. Mater.*, 2006, **18**, 2325-2329.
131. H. Wu, G. Chan, J. W. Choi, I. Ryu, Y. Yao, M. T. McDowell, S. W. Lee, A. Jackson, Y. Yang, L. B. Hu and Y. Cui, *Nat. Nanotechnol.*, 2012, **7**, 309-314.
132. W. J. Zhang, *J. Power. Sources*, 2011, **196**, 13-24.
133. W. M. Zhang, J. S. Hu, Y. G. Guo, S. F. Zheng, L. S. Zhong, W. G. Song and L. J. Wan, *Adv. Mater.*, 2008, **20**, 1160-1165.
134. J. K. Lee, K. B. Smith, C. M. Hayner and H. H. Kung, *Chem. Commun.*, 2010, **46**, 2025-2027.
135. Z. Li, J. Ding, H. Wang, K. Cui, T. Stephenson, D. Karpuзов and D. Mitlin, *Nano Energy*, 2015, **15**, 369-378.
136. H. Tang, J. Zhang, Y. J. Zhang, Q. Q. Xiong, Y. Y. Tong, Y. Li, X. L. Wang, C. D. Gu and J. P. Tu, *J. Power. Sources*, 2015, **286**, 431-437.
137. J. Meng, Y. Cao, Y. Suo, Y. Liu, J. Zhang and X. Zheng, *Electrochim. Acta*, 2015, **176**, 1001-1009.
138. J. Qin, C. N. He, N. Q. Zhao, Z. Y. Wang, C. S. Shi, E. Z. Liu and J. J. Li, *ACS Nano*, 2014, **8**, 1728-1738.
139. D. Aurbach, Z. Lu, A. Schechter, Y. Gofer, H. Gizbar, R. Turgeman, Y. Cohen, M. Moshkovich and E. Levi, *Nature*, 2000, **407**, 724-727.
140. M. D. Slater, D. Kim, E. Lee and C. S. Johnson, *Adv. Funct. Mater.*, 2013, **23**, 947-958.
141. M. C. Lin, M. Gong, B. G. Lu, Y. P. Wu, D. Y. Wang, M. Y. Guan, M. Angell, C. X. Chen, J. Yang, B. J. Hwang and H. J. Dai, *Nature*, 2015, **520**, 325-328.
142. J. Xu, M. Wang, N. P. Wickramaratne, M. Jaroniec, S. Dou and L. Dai, *Adv. Mater.*, 2015, **27**, 2042-2048.
143. Q. An, Y. Li, H. Deog Yoo, S. Chen, Q. Ru, L. Mai and Y. Yao, *Nano Energy*, 2015, **18**, 265-272.
144. A. S. Arico, P. Bruce, B. Scrosati, J. M. Tarascon and W. Van Schalkwijk, *Nat. Mater.*, 2005, **4**, 366-377.
145. L. Schlapbach and A. Zuttel, *Nature*, 2001, **414**, 353-358.
146. L. J. Murray, M. Dinca and J. R. Long, *Chem. Soc. Rev.*, 2009, **38**, 1294-1314.
147. S. Gadielli and Z. X. Guo, *Prog. Mater. Sci.*, 2015, **69**, 1-60.
148. S. Patchkovskii, J. S. Tse, S. N. Yurchenko, L. Zhechkov, T. Heine and G. Seifert, *Proc. Natl. Acad. Sci. U. S. A.*, 2005, **102**, 10439-10444.
149. G. K. Dimitrakakis, E. Tylianakis and G. E. Froudakis, *Nano Lett.*, 2008, **8**, 3166-3170.
150. G. Kim and S. H. Jhi, *J. Phys. Chem. C*, 2009, **113**, 20499-20503.
151. J. Zhu, X. Yang, Z. Fu, J. He, C. Wang, W. Wu and L. Zhang, *Chem. – Eur. J.*, 2016, **22**, 2515-2524.
152. L. F. Cabeza, A. Castell, C. Barreneche, A. de Gracia

Journal Name

ARTICLE

- and A. I. Fernandez, *Renew. Sust. Energ. Rev.*, 2011, **15**, 1675-1695.
153. E. Pop, V. Varshney and A. K. Roy, *MRS Bull.*, 2012, **37**, 1273-1281.
154. Z. Yan, G. X. Liu, J. M. Khan and A. A. Balandin, *Nat. Commun.*, 2012, **3**, 8.
155. A. A. Balandin, S. Ghosh, W. Z. Bao, I. Calizo, D. Teweldebrhan, F. Miao and C. N. Lau, *Nano Lett.*, 2008, **8**, 902-907.
156. A. A. Balandin, *Nat. Mater.*, 2011, **10**, 569-581.
157. J. Yang, E. Zhang, X. Li, Y. Zhang, J. Qu and Z.-Z. Yu, *Carbon*, 2016, **98**, 50-57.
158. Y. Zhong, M. Zhou, F. Huang, T. Lin and D. Wan, *Sol. Energ. Mat. Sol. C.*, 2013, **113**, 195-200.
159. M. Zhou, T. Lin, F. Huang, Y. Zhong, Z. Wang, Y. Tang, H. Bi, D. Wan and J. Lin, *Adv. Funct. Mater.*, 2013, **23**, 2263-2269.
160. S. Ye, Q. Zhang, D. Hu and J. Feng, *J. Mater. Chem. A*, 2015, **3**, 4018-4025.
161. Y. Jiao, Y. Zheng, M. T. Jaroniec and S. Z. Qiao, *Chem. Soc. Rev.*, 2015, **44**, 2060-2086.
162. B. C. H. Steele and A. Heinzel, *Nature*, 2001, **414**, 345-352.
163. N. Mahmood, C. Z. Zhang, H. Yin and Y. L. Hou, *J. Mater. Chem. A*, 2014, **2**, 15-32.
164. A. Chandan, M. Hattenberger, A. El-Kharouf, S. F. Du, A. Dhir, V. Self, B. G. Pollet, A. Ingram and W. Bujalski, *J. Power. Sources*, 2013, **231**, 264-278.
165. Z. Yang, H. G. Nie, X. Chen, X. H. Chen and S. M. Huang, *J. Power. Sources*, 2013, **236**, 238-249.
166. W. W. Li, H. Q. Yu and Z. He, *Energy Environ. Sci.*, 2014, **7**, 911-924.
167. Y. J. Wang, J. L. Qiao, R. Baker and J. J. Zhang, *Chem. Soc. Rev.*, 2013, **42**, 5768-5787.
168. C. H. Cui, L. Gan, M. Heggen, S. Rudi and P. Strasser, *Nat. Mater.*, 2013, **12**, 765-771.
169. J. B. Wu and H. Yang, *Acc. Chem. Res.*, 2013, **46**, 1848-1857.
170. T. Y. Ma, S. Dai, M. Jaroniec and S. Z. Qiao, *J. Am. Chem. Soc.*, 2014, **136**, 13925-13931.
171. G. Wu and P. Zelenay, *Acc. Chem. Res.*, 2013, **46**, 1878-1889.
172. L. M. Dai, Y. H. Xue, L. T. Qu, H. J. Choi and J. B. Baek, *Chem. Rev.*, 2015, **115**, 4823-4892.
173. R. Silva, D. Voiry, M. Chhowalla and T. Asefa, *J. Am. Chem. Soc.*, 2013, **135**, 7823-7826.
174. K. P. Gong, F. Du, Z. H. Xia, M. Durstock and L. M. Dai, *Science*, 2009, **323**, 760-764.
175. L. T. Qu, Y. Liu, J. B. Baek and L. M. Dai, *ACS Nano*, 2010, **4**, 1321-1326.
176. M. Wang, J. Wang, Y. Hou, D. Shi, D. Wexler, S. D. Poynton, R. C. Slade, W. Zhang, H. Liu and J. Chen, *ACS Appl. Mater. Interfaces*, 2015, **7**, 7066-7072.
177. C. Xu, Y. Su, D. Liu and X. He, *Phys. Chem. Chem. Phys.*, 2015, **17**, 25440-25448.
178. D. Yu, L. Wei, W. Jiang, H. Wang, B. Sun, Q. Zhang, K. Goh, R. Si and Y. Chen, *Nanoscale*, 2013, **5**, 3457-3464. [View Article Online](#)
179. L. Chen, C. Y. Xu, R. Du, Y. Y. Mao, C. Xue, L. M. Chen, L. T. Qu, J. Zhang and T. Yi, *J. Mater. Chem. A*, 2015, **3**, 5617-5627.
180. X. Fu, J. Y. Choi, P. Zamani, G. Jiang, M. A. Hoque, F. M. Hassan and Z. Chen, *ACS Appl. Mater. Interfaces*, 2016, **8**, 6488-6495.
181. H. Yin, C. Zhang, F. Liu and Y. Hou, *Adv. Funct. Mater.*, 2014, **24**, 2930-2937.
182. Q. Huang, F. Tao, L. Zou, T. Yuan, Z. Zou, H. Zhang, X. Zhang and H. Yang, *Electrochim. Acta*, 2015, **152**, 140-145.
183. Z. Luo, C. Tan, X. Zhang, J. Chen, X. Cao, B. Li, Y. Zong, L. Huang, X. Huang, L. Wang, W. Huang and H. Zhang, *Small*, 2016, **12**, 5920-5926.
184. W. Han, L. Ren, L. Gong, X. Qi, Y. Liu, L. Yang, X. Wei and J. Zhong, *ACS Sustain. Chem. Eng.*, 2014, **2**, 741-748.
185. F. E. Osterloh, *Chem. Mat.*, 2008, **20**, 35-54.
186. G. Girishkumar, B. McCloskey, A. C. Luntz, S. Swanson and W. Wilcke, *J. Phys. Chem. Lett.*, 2010, **1**, 2193-2203.
187. Y. Umena, K. Kawakami, J. R. Shen and N. Kamiya, *Nature*, 2011, **473**, 55-U65.
188. Y. Lee, J. Suntivich, K. J. May, E. E. Perry and Y. Shao-Horn, *J. Phys. Chem. Lett.*, 2012, **3**, 399-404.
189. W. Yan, X. Cao, J. Tian, C. Jin, K. Ke and R. Yang, *Carbon*, 2016, **99**, 195-202.
190. S. Mao, Z. Wen, T. Huang, Y. Hou and J. Chen, *Energy Environ. Sci.*, 2014, **7**, 609-616.
191. J. Zhang, Z. Zhao, Z. Xia and L. Dai, *Nat. Nanotechnol.*, 2015, **10**, 444-452.
192. H. B. Yang, J. Miao, S.-F. Hung, J. Chen, H. B. Tao, X. Wang, L. Zhang, R. Chen, J. Gao, H. M. Chen, L. Dai and B. Liu, *Sci. Adv.*, 2016, **2**, e1501122.
193. B. Hinnemann, P. G. Moses, J. Bonde, K. P. Jorgensen, J. H. Nielsen, S. Horch, I. Chorkendorff and J. K. Norskov, *J. Am. Chem. Soc.*, 2005, **127**, 5308-5309.
194. J. H. Wang, W. Cui, Q. Liu, Z. C. Xing, A. M. Asiri and X. P. Sun, *Adv. Mater.*, 2016, **28**, 215-230.
195. H. Y. Jin, J. Wang, D. F. Su, Z. Z. Wei, Z. F. Pang and Y. Wang, *J. Am. Chem. Soc.*, 2015, **137**, 2688-2694.
196. Y. Zhao, F. Zhao, X. Wang, C. Xu, Z. Zhang, G. Shi and L. Qu, *Angew. Chem., Int. Ed.*, 2014, **53**, 13934-13939.
197. Y. G. Li, H. L. Wang, L. M. Xie, Y. Y. Liang, G. S. Hong and H. J. Dai, *J. Am. Chem. Soc.*, 2011, **133**, 7296-7299.
198. C. L. Tan and H. Zhang, *Chem. Soc. Rev.*, 2015, **44**, 2713-2731.
199. W. Zhou, K. Zhou, D. Hou, X. Liu, G. Li, Y. Sang, H. Liu, L. Li and S. Chen, *ACS Appl. Mater. Interfaces*, 2014, **6**, 21534-21540.
200. Y. Zhao, X. Xie, J. Zhang, H. Liu, H. J. Ahn, K. Sun and G. Wang, *Chem. Eur. J.*, 2015, **21**, 15908-15913.
201. Z. Li, X. Dai, K. Du, Y. Ma, M. Liu, H. Sun, X. Ma and X. Zhang, *J. Phys. Chem. C*, 2016, **120**, 1478-1487.
202. X. Zhang, Y. Han, L. Huang and S. Dong,

ARTICLE

Journal Name

203. *ChemSusChem*, 2016, **9**, 3049-3053.

204. A. Han, S. Jin, H. Chen, H. Ji, Z. Sun and P. Du, *J. Mater. Chem. A*, 2015, **3**, 1941-1946.

205. J. G. Yu, J. X. Low, W. Xiao, P. Zhou and M. Jaroniec, *J. Am. Chem. Soc.*, 2014, **136**, 8839-8842.

206. W. G. Tu, Y. Zhou and Z. G. Zou, *Adv. Mater.*, 2014, **26**, 4607-4626.

207. R. Kuriki, H. Matsunaga, T. Nakashima, K. Wada, A. Yamakata, O. Ishitani and K. Maeda, *J. Am. Chem. Soc.*, 2016, **138**, 5159-5170.

208. F. Marino, C. Descorme and D. Duprez, *App. Catal. B-Environ.*, 2005, **58**, 175-183.

209. Y. M. He, L. H. Zhang, B. T. Teng and M. H. Fan, *Environ. Sci. Technol.*, 2015, **49**, 649-656.

210. J. Wu, M. Liu, P. P. Sharma, R. M. Yadav, L. Ma, Y. Yang, X. Zou, X. D. Zhou, R. Vajtai, B. I. Yakobson, J. Lou and P. M. Ajayan, *Nano Lett.*, 2016, **16**, 466-470.

211. C. Y. Zhai, M. S. Zhu, F. Z. Pang, D. Bin, C. Lu, M. C. Goh, P. Yang and Y. K. Du, *ACS Appl. Mater. Interfaces*, 2016, **8**, 5972-5980.

212. M. E. Scofield, C. Koenigsmann, L. Wang, H. Q. Liu and S. S. Wong, *Energy Environ. Sci.*, 2015, **8**, 350-363.

213. S. P. S. Badwal, S. Giddey, A. Kulkarni, J. Goel and S. Basu, *Appl. Energy*, 2015, **145**, 80-103.

214. J. Duan, X. Zhang, W. Yuan, H. Chen, S. Jiang, X. Liu, Y. Zhang, L. Chang, Z. Sun and J. Du, *J. Power. Sources*, 2015, **285**, 76-79.

215. C.-H. A. Tsang, K. N. Hui, K. S. Hui and L. Ren, *J. Mater. Chem. A*, 2014, **2**, 17986-17993.

216. G. H. Yang, Y. Z. Zhou, H. B. Pan, C. Z. Zhu, S. F. Fu, C. M. Wai, D. Du, J. J. Zhu and Y. H. Lin, *Ultrason. Sonochem.*, 2016, **28**, 192-198.

217. H. S. Liu, C. J. Song, L. Zhang, J. J. Zhang, H. J. Wang and D. P. Wilkinson, *J. Power Sources*, 2006, **155**, 95-110.

218. S. Zhao, H. Yin, L. Du, G. Yin, Z. Tang and S. Liu, *J. Mater. Chem. A*, 2014, **2**, 3719.

219. L. Ren, K. S. Hui and K. N. Hui, *J. Mater. Chem. A*, 2013, **1**, 5689.

220. B. E. Logan, B. Hamelers, R. A. Rozendal, U. Schrorder, J. Keller, S. Freguia, P. Aelterman, W. Verstraete and K. Rabaey, *Environ. Sci. Technol.*, 2006, **40**, 5181-5192.

221. H. L. Tang, S. C. Cai, S. L. Xie, Z. B. Wang, Y. X. Tong, M. Pan and X. H. Lu, *Adv. Sci.*, 2016, **3**, 8.

222. R. Burkitt, T. R. Whiffen and E. H. Yu, *App. Catal. B-Environ.*, 2016, **181**, 279-288.

223. S. J. You, X. B. Gong, W. Wang, D. P. Qi, X. H. Wang, X. D. Chen and N. Q. Ren, *Adv. Energy Mater.*, 2016, **6**, 9.

224. Y. Z. Zhang, G. Q. Mo, X. W. Li, W. D. Zhang, J. Q. Zhang, J. S. Ye, X. D. Huang and C. Z. Yu, *J. Power. Sources*, 2011, **196**, 5402-5407.

225. Y. Hou, B. Zhang, Z. Wen, S. Cui, X. Guo, Z. He and J. Chen, *J. Mater. Chem. A*, 2014, **2**, 13795.

226. S. Zhao, Y. Li, H. Yin, Z. Liu, E. Luan, F. Zhao, Z. Tang and S. Liu, *Sci. Adv.*, 2015, **1**, e1500372.

227. J. S. Luo, J. H. Im, M. T. Mayer, M. Schreier, M. K. Nazeeruddin, N. G. Park, S. D. Tilley, H. J. Fan and M. Gratzel, *Science*, 2014, **345**, 1593-1596.

228. Q. Wang, T. Hisatomi, Q. X. Jia, H. Tokudome, M. Zhong, C. Z. Wang, Z. H. Pan, T. Takata, M. Nakabayashi, N. Shibata, Y. B. Li, I. D. Sharp, A. Kudo, T. Yamada and K. Domen, *Nat. Mater.*, 2016, **15**, 611-615.

229. G. G. Zhang, Z. A. Lan, L. H. Lin, S. Lin and X. C. Wang, *Chem. Sci.*, 2016, **7**, 3062-3066.

230. J. Gu, Y. Yan, J. L. Young, K. X. Steirer, N. R. Neale and J. A. Turner, *Nat. Mater.*, 2016, **15**, 456-460.

231. Y. Hou, Z. Wen, S. Cui, X. Feng and J. Chen, *Nano Lett.*, 2016, **16**, 2268-2277.

232. D. Kim, K. K. Sakimoto, D. C. Hong and P. D. Yang, *Angew. Chem., Int. Ed.*, 2015, **54**, 3259-3266.

233. K. K. Sakimoto, A. B. Wong and P. D. Yang, *Science*, 2016, **351**, 74-77.

234. M. A. Green, K. Emery, Y. Hishikawa, W. Warta and E. D. Dunlop, *Prog. Photovoltaics*, 2015, **23**, 1-9.

235. K. Kakiage, Y. Aoyama, T. Yano, K. Oya, J. Fujisawab and M. Hanaya, *Chem. Commun.*, 2015, **51**, 15894-15897.

236. J. H. Wu, Z. Lan, J. M. Lin, M. L. Huang, Y. F. Huang, L. Q. Fan and G. G. Luo, *Chem. Rev.*, 2015, **115**, 2136-2173.

237. H. Wang, K. Sun, F. Tao, D. J. Stacchiola and Y. H. Hu, *Angew. Chem., Int. Ed.*, 2013, **52**, 9210-9214.

238. H. J. Ahn, I. H. Kim, J. C. Yoon, S. I. Kim and J. H. Jang, *Chem. Commun.*, 2014, **50**, 2412-2415.

239. Y. Xue, J. Liu, H. Chen, R. Wang, D. Li, J. Qu and L. Dai, *Angew. Chem., Int. Ed.*, 2012, **51**, 12124-12127.

240. H. N. Kim, H. Yoo and J. H. Moon, *Nanoscale*, 2013, **5**, 4200-4204.

241. A. Yella, H. W. Lee, H. N. Tsao, C. Y. Yi, A. K. Chandiran, M. K. Nazeeruddin, E. W. G. Diau, C. Y. Yeh, S. M. Zakeeruddin and M. Gratzel, *Science*, 2011, **334**, 629-634.

242. S. Yuan, Q. Tang, B. He and Y. Zhao, *J. Power Sources*, 2014, **260**, 225-232.

243. W. S. Yang, J. H. Noh, N. J. Jeon, Y. C. Kim, S. Ryu, J. Seo and S. I. Seok, *Science*, 2015, **348**, 1234-1237.

244. N. J. Jeon, J. H. Noh, W. S. Yang, Y. C. Kim, S. Ryu, J. Seo and S. I. Seok, *Nature*, 2015, **517**, 476-480.

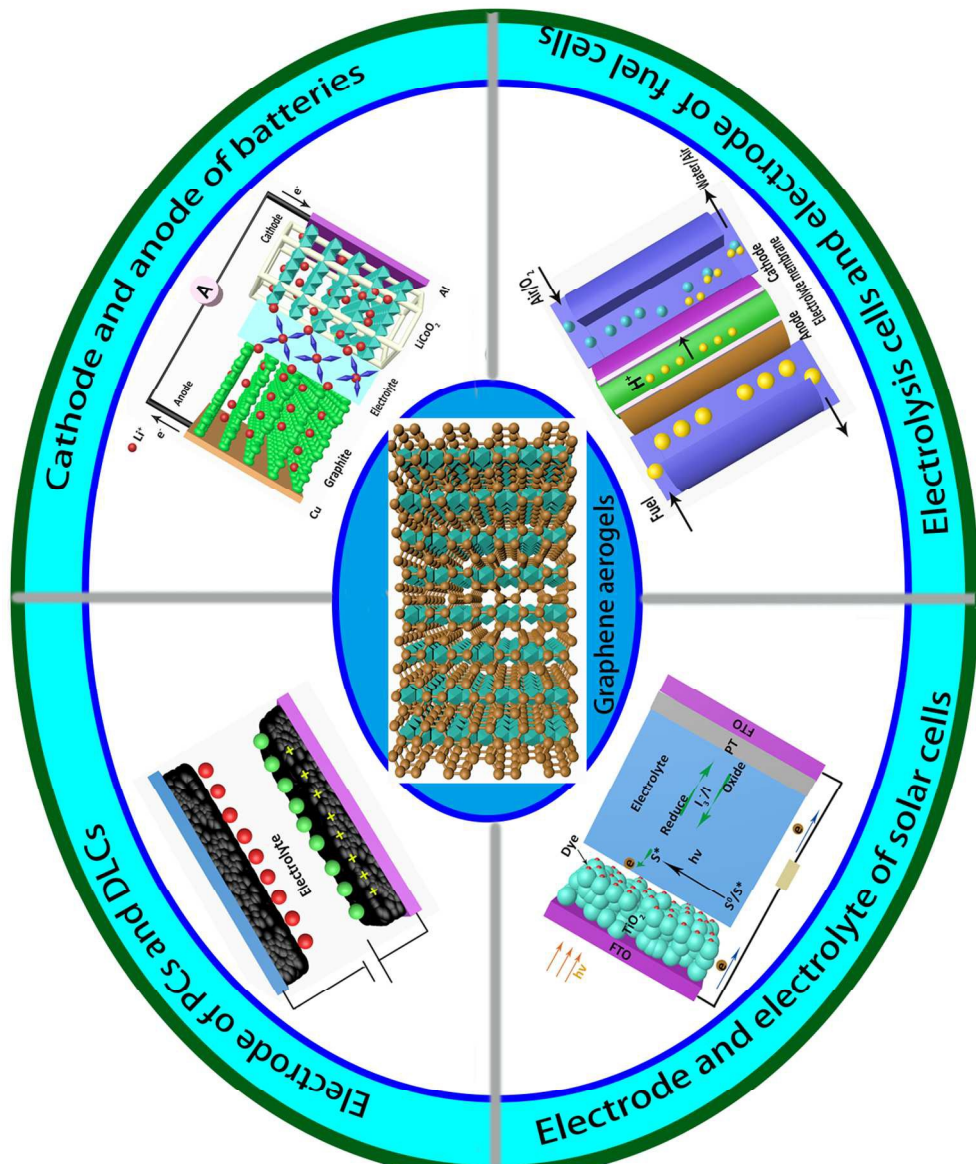
245. D. P. McMeekin, G. Sadoughi, W. Rehman, G. E. Eperon, M. Saliba, M. T. Horantner, A. Haghhighirad, N. Sakai, L. Korte, B. Rech, M. B. Johnston, L. M. Herz and H. J. Snaith, *Science*, 2016, **351**, 151-155.

246. K. A. Bush, A. F. Palmstrom, Z. S. J. Yu, M. Boccard, R. Cheacharoen, J. P. Mailoa, D. P. McMeekin, R. L. Z. Hoye, C. D. Bailie, T. Leijtens, I. M. Peters, M. C. Minichetti, N. Rolston, R. Prasanna, S. Sofia, D. Harwood, W. Ma, F. Moghadam, H. J. Snaith, T. Buonassisi, Z. C. Holman, S. F. Bent and M. D.

Journal Name

ARTICLE

- McGehee, *Nat. Energy*, 2017, **2**, 7.
247. O. Ergen, S. M. Gilbert, T. Pham, S. J. Turner, M. T. Z. Tan, M. A. Worsley and A. Zettl, *Nat. Mater.*, 2017, **16**, 522-525.
248. L. Zhang, F. Zhang, X. Yang, G. K. Long, Y. P. Wu, T. F. Zhang, K. Leng, Y. Huang, Y. F. Ma, A. Yu and Y. S. Chen, *Sci. Rep.*, 2013, **3**, 9.
249. Y. M. He, W. J. Chen, X. D. Li, Z. X. Zhang, J. C. Fu, C. H. Zhao and E. Q. Xie, *ACS Nano*, 2013, **7**, 174-182.
250. J. Y. Ji, L. L. Zhang, H. X. Ji, Y. Li, X. Zhao, X. Bai, X. B. Fan, F. B. Zhang and R. S. Ruoff, *ACS Nano*, 2013, **7**, 6237-6243.
251. Z. Y. Zhang, F. Xiao, Y. L. Guo, S. Wang and Y. Q. Liu, *ACS Appl. Mater. Interfaces*, 2013, **5**, 2227-2233.
252. X. C. Dong, Y. F. Cao, J. Wang, M. B. Chan-Park, L. H. Wang, W. Huang and P. Chen, *RSC Adv.*, 2012, **2**, 4364-4369.
253. B. You, L. L. Wang, L. Yao and J. Yang, *Chem. Commun.*, 2013, **49**, 5016-5018.
254. W. Wang, S. R. Guo, M. Penchev, I. Ruiz, K. N. Bozhilov, D. Yan, M. Ozkan and C. S. Ozkan, *Nano Energy*, 2013, **2**, 294-303.
255. J. Zhi, W. Zhao, X. Y. Liu, A. R. Chen, Z. Q. Liu and F. Q. Huang, *Adv. Funct. Mater.*, 2014, **24**, 2013-2019.
256. Y. Liu, X. Y. Cai and W. D. Shi, *Mater. Lett.*, 2016, **172**, 72-75.
257. D. Xie, W. J. Tang, X. H. Xia, D. H. Wang, D. Zhou, F. Shi, X. L. Wang, C. D. Gu and J. P. Tu, *J. Power Sources*, 2015, **296**, 392-399.
258. M. P. Yu, A. J. Wang, Y. S. Wang, C. Li and G. Q. Shi, *Nanoscale*, 2014, **6**, 11419-11424.
259. J. Wang, J. L. Liu, D. L. Chao, J. X. Yan, J. Y. Lin and Z. X. Shen, *Adv. Mater.*, 2014, **26**, 7162-7169.
260. J. Ji, H. Ji, L. Zhang, X. Zhao, X. Bai, X. Fan, F. Zhang and R. Ruoff, *Adv. Mater.*, 2013, **25**, 4673-4677.
261. Z. Li, J. Ding, H. L. Wang, K. Cui, T. Stephenson, D. Karpuzov and D. Mitlin, *Nano Energy*, 2015, **15**, 369-378.



488x593mm (72 x 72 DPI)

Broader context

Environmental pollution caused by the rapid consumption of fossil fuels has prompted investigation into alternative sources of efficient, cost-effective, and sustainable energy systems. Traditionally, noble metals and transition-metal oxides are the most widely used electrode materials. However, their high price and associated toxicity hinder further development. The combination of the chemical properties and 3D network morphology which ensure excellent electron transport performance make graphene aerogels (GAs) ideal candidates for various future energy storage and conversion systems, e.g., supercapacitors, Li-batteries, fuel cells and solar cells. Moreover, the ultralow density and flexibility of 3D aerogels are beneficial for portable equipment and roll-to-roll processing. This review will briefly outline and compare various fabrication methods of GAs and detail the roles of GAs in energy systems. In addition, we will look into some critical engineering strategies that give rise to the electrochemical properties of 3D GAs such as enlarged surface area, tailored porosity, efficient separation of carriers, and chemical/physical modification. The creative points and trends detailed in this review will offer promising development directions for aerogels and other porous network structures as well as metal-free materials in energy storage and conversion systems.